J. Fluid Mech. (2019), *vol.* 861, *pp.* 901–929.
doi:10.1017/jfm.2018.936

Modulation of the turbulence regeneration cycle by inertial particles in planar Couette flow

G. Wang[1,†] **and D. H. Richter**[1,†]

[1]Department of Civil and Environmental Engineering and Earth Sciences, University of Notre Dame, Notre Dame, IN 46556, USA

(Received 3 July 2018; revised 27 September 2018; accepted 15 November 2018; first published online 28 December 2018)

Two-way coupled direct numerical simulations are used to investigate the effects of inertial particles on self-sustained, turbulent coherent structures (i.e. the so-called regeneration cycle) in plane Couette flow at low Reynolds number just above the onset of transition. Tests show two limiting behaviours with increasing particle inertia, similar to the results from previous linear stability analyses: low-inertia particles trigger the laminar-to-turbulent instability whereas high-inertia particles tend to stabilize turbulence due to the extra dissipation induced by particle–fluid coupling. Furthermore, it is found that the streamwise coupling between phases is the dominant factor in damping of the turbulence and is highly related to the spatial distribution of the particles. The presence of particles in different turbulent coherent structures (large-scale vortices or large-scale streaks) determines the turbulent kinetic energy of particulate phase, which is related to the particle response time scaled by the turnover time of large-scale vortices. By quantitatively investigating the periodic character of the whole regeneration cycle and the phase difference between linked sub-steps, we show that the presence of inertial particles does not alter the periodic nature of the cycle or the relative length of each of the sub-steps. Instead, high-inertia particles greatly weaken the large-scale vortices as well as the streamwise vorticity stretching and lift-up effects, thereby suppressing the fluctuating amplitude of the large-scale streaks. The primary influence of low-inertia particles, however, is to strengthen the large-scale vortices, which fosters the cycle and ultimately reduces the critical Reynolds number.

Key words: multiphase flow, particle/fluid flow, turbulence simulation

1. Introduction

Turbulence in the atmospheric boundary layer is responsible for the dispersion of pollutants, dust, sand and other constituents (Garratt 1994). However, even with dilute volume concentrations, turbulence modulation by particles still poses a formidable challenge to fully understanding how these constituents alter their own transport (Balachandar & Eaton 2010). Turbulence in the atmospheric boundary layer is characterized by very high Reynolds numbers, and is therefore subject to the numerous interactions between inner and outer layers, including the dynamics of the so-called

† Email addresses for correspondence: gwang4@nd.edu, David.Richter.26@nd.edu

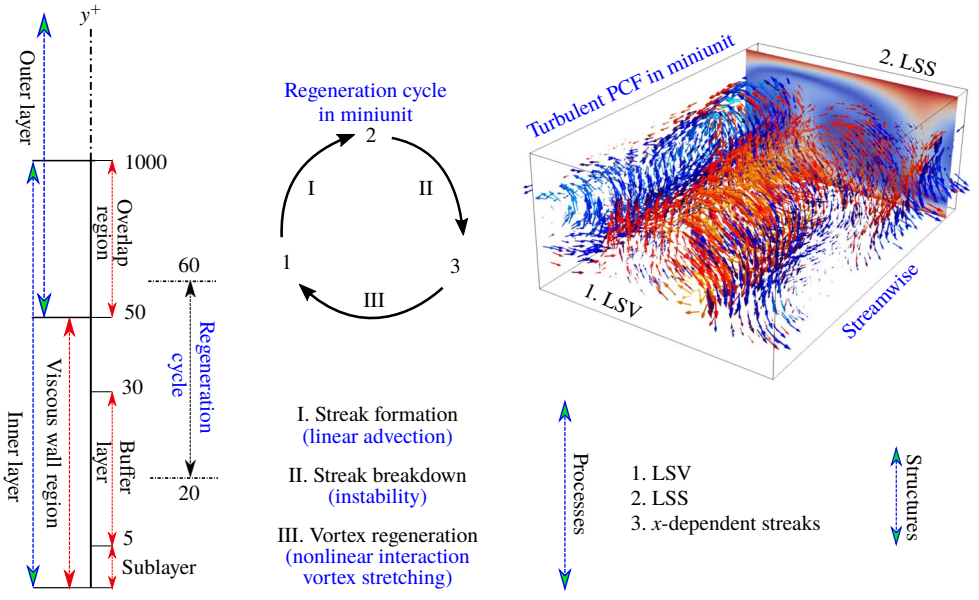

FIGURE 1. (Colour online) Sketch of various wall regions and boundary layers in wall units (Jiménez & Pinelli 1999; Pope 2000) and the regeneration cycle sub-steps (Hamilton *et al.* 1995; Waleffe 1997; Schoppa & Hussain 2002) in a domain size called 'minimal' unit. In the top-right is the flow field in turbulent PCF in miniunit. Large-scale vortex (LSV) is shown by vector fields and coloured by the streamwise vorticity. Large-scale streak (LSS) is shown by the contour of the streamwise velocity magnitude.

very-large-scale motions which develop (Smits, McKeon & Marusic 2011; Inoue *et al.* 2012; Jiménez 2018). Since in many atmospheric multiphase flows the dispersed phase is emitted from a surface (e.g. sand saltation, bubbles bursting at a water surface), the effect of particulates on inner–outer interactions and more specifically on the regeneration cycles of near-wall coherent motions is the primary interest of the present study. While the complexity of high-Reynolds-number, multiphase, turbulent flows is high due in large part to the wide range of relevant spatial and temporal scales, the present aim is to simplify the problem and examine one key aspect of the larger picture: the regeneration cycle of coherent structures in the overlap region of wall-bounded turbulence. In this regard, turbulent plane Couette flow (PCF) at low Reynolds number is known to contain the self-sustained processes exhibited by turbulent coherent structures (Hamilton, Kim & Waleffe 1995; Waleffe 1997), as well as large-scale structures interacting with smaller near-wall motions (Komminaho, Lundbladh & Johansson 1996; Kitoh, Nakabyashi & Nishimura 2005). This set-up is therefore a representative, computationally inexpensive candidate for shedding light on particle transport and the fundamental modification of the regeneration cycle and inner/outer interactions.

It is commonly accepted that the full regeneration cycle in the inner layer exhibits the main characteristics of turbulence (Hamilton *et al.* 1995; Waleffe 1997; Jiménez & Pinelli 1999; Kawahara & Kida 2001; Schoppa & Hussain 2002). Figure 1 provides a schematic of the various regions near the wall, as well as the key turbulent structures and processes which make up the regeneration cycle in the region of $20 < y^+ < 60$; see Waleffe (1997) and Jiménez & Pinelli (1999). This self-sustained regeneration cycle is

marked by three important structures: large-scale vortices (LSVs), large-scale streaks (LSSs) and x-dependent meandering streaks; each stage of the regeneration process is associated with sequential sub-processes. Specifically, the streaks are generated by a linear process, the so-called lift-up effect, whereas the following two processes are the result of nonlinear interactions called streak breakdown and vortex regeneration. The regeneration cycle was first investigated by Hamilton *et al.* (1995) in PCF using a so-called 'miniunit' configuration, which is the minimal geometric domain that is sufficient to accommodate the self-sustained flow structures for single-phase turbulence. This minimal simulation domain was carefully examined in Couette flow configuration by Hamilton *et al.* (1995) and pressure-driven flow by Jiménez & Moin (1991). In both cases, the spanwise length is slightly larger than 100 wall units, which corresponds to the spanwise characteristic spacing between two coherent structures.

The modulation of the regeneration cycle has been found to be related to the spatial distribution of a particulate phase. In fully resolved simulations with finite-sized, neutrally buoyant particles, the cycle is promoted in turbulent pressure-driven flow, and is hardly modified in turbulent PCF (Brandt 2014; Wang, Abbas & Climent 2018). In the case of PCF, particles are more likely to be present in the core of the large-scale rolls which are mainly responsible for dissipating energy. The same phenomenon is also observed experimentally in Taylor–Couette flow (Majji, Banerjee & Morris 2018) if the particle concentration is low and and the particles are relatively small compared with the gap. However, in pressure-driven flow, finite-size neutrally buoyant particles show a non-monotonic effect on laminar-to-turbulent transition. From an experiment of particle-laden, pressure-driven pipe flow, Matas, Morris & Guazzelli (2003) found that low volume concentrations (less than 20 %) of large particles (particle to pipe diameter ratio of around $1/20$) sustain the turbulent state and decrease the transition threshold, whereas a high concentration of small particles advances the transition threshold significantly. Wang *et al.* (2018) further found that particles tend to trigger instability in pressure-driven flow due to the particles' preferential presence in near-wall streaks.

In general, turbulence modulation is found to depend on the size ratio between the particle and turbulence length scales, and on the time scale ratio between the particle response time with a characteristic time scale of the flow – i.e. the dimensionless Stokes number St (Gore & Crowe 1989; Elghobashi 1994). Gore & Crowe (1989), for instance, proposed a relationship of size ratio between particle diameter and the flow integral length scale to flow turbulent intensity attenuation/augmentation. Tanaka & Eaton (2008) formulated a dimensionless particle momentum number to predict turbulence modulation which includes the flow microscale (Kolmogorov scale), the energy-containing scale, as well as the Stokes number. At high Reynolds number, Tanaka & Eaton (2008) divided the turbulent modification into three regions: moderate momentum number tends to attenuate the turbulence whereas low or high momentum number tend to augment the turbulence. For heavy particles which can be reasonably modelled using only a drag force (i.e. neglecting lift, added mass and Basset history terms; see Maxey & Riley (1983)), Balachandar & Eaton (2010) proposed that the turbulence modulation mechanisms can be simplified: turbulence reduction comes from enhanced inertia and increased dissipation arising from particle drag, whereas the turbulence enhancement is due to enhanced velocity fluctuation from wake dynamics. A large body of work on turbulent kinetic energy modification (Squires & Eaton 1990; Elghobashi & Truesdell 1993; Pan & Banerjee 1996; Burton & Eaton 2005), interphasial energy transfer (Zhao, Andersson & Gillissen 2013), particle transfer and segregation (Marchioli & Soldati 2002) or drag reduction (Li *et al.* 2001; Dritselis & Vlachos 2008) can be found in the literature.

While we are ultimately interested in the modulation of high-Reynolds-number wall turbulence due to inertial particles, our specific focus in this work is on the modification of the near-wall regeneration cycle and its close connection with laminar-to-turbulent transition as a model for inner–outer interactions; this influence of a dispersed phase in turbulent flows has received relatively little attention. At Reynolds numbers close to the onset of transition, Klinkenberg, De Lange & Brandt (2011) proposed a stability Stokes number, where at small values (fine particles) the critical Reynolds number decreases proportionally to the particle mass fraction, and where at intermediate values yields an increase of the critical Reynolds number, the enhancement is proportional to the volume fraction. Through linear analysis of the Orr–Sommerfeld equation coupled to a dispersed phase via drag, Saffman (1962) theoretically predicted that fine particles tend to destabilize the gas flow whereas coarse particles have a stabilizing action. The drag coupling between phases therefore has competing effects: low-inertia particles tend to destabilize the flow by adding to the effective density of the gas, and high-inertia particles tend to act as an extra dissipation source, thereby stabilizing the flow. Following the formulation proposed by Saffman (1962), Michael (1964), Rudyak, Isakov & Bord (1997) and Klinkenberg *et al.* (2011) numerically solved the modified Orr–Sommerfeld equation for plane Poiseuille flow. Michael (1964) showed an increased critical Reynolds number at low particle concentration whereas Rudyak *et al.* (1997) and Klinkenberg *et al.* (2011) found that the critical Reynolds number reaches a maximum and then decreases gradually with increasing particle relaxation time.

Other configurations have also been theoretically predicted: Dimas & Kiger (1998) studied a particle-laden mixing layer and DeSpirito & Wang (2001) analysed a particle-laden jet. A similar conclusion is drawn that small, low-inertia particles induce a destabilization effect whereas large-Stokes-number particles stabilize, and that the effect is approximately proportional to the particle mass loading (at least in dilute concentrations). For these stability analyses, however, the particles often must be assumed to be homogeneously distributed or distributed with an assumed profile; nonlinear effects such as particle preferential accumulation and the dynamics of the near-wall regeneration cycles are difficult to include in the analysis. Some nonlinear studies on transition do exist, including those of Klinkenberg *et al.* (2011, 2013), who also find that small inertia tends to decrease the critical Reynolds number whereas particles with intermediate Stokes numbers increase the critical Reynolds number. From dilute limit to high mass loading, Capecelatro, Desjardins & Fox (2018) find that fluid-phase turbulence kinetic energy is generated by mean-shear production in dilute limit ($\overline{\Phi_m} \leqslant 1$), whereas it is entirely generated by drag production at high mass loading ($\overline{\Phi_m} \geqslant 10$). In the intermediate regime ($2 \leqslant \overline{\Phi_m} \leqslant 4$), the flow relaminarizes due to higher rate of dissipation compared to production of turbulence kinetic energy. Mechanisms regarding the disruption of turbulence regeneration, however, are still an open question.

To study the particle-induced modulation of the self-sustained regeneration cycle in wall turbulence, numerical simulations are performed for particle suspensions in PCF in a 'miniunit' domain. In previous work, finite-size particles with low Stokes number are found to hardly modify the regeneration cycle due to particles preferentially accumulating in the LSVs (Wang *et al.* 2018). At a higher Reynolds number, however, pointwise inertial particles with moderate to high Stokes numbers preferentially 'operate' on flow structure scales associated with the particle response time scale (Richter & Sullivan 2013, 2014; Richter 2015), but this effect on the regeneration cycle remains unclear. While these previous simulations of particle-laden

turbulent flows have identified numerous modifications to the flow statistics, energy spectra and coherent structures, the dynamical processes behind these modifications have not been analysed in detail. Therefore a primary purpose of this work is to link our existing knowledge of particle-laden turbulence modification with the flow dynamics via modifications to the near-wall regeneration cycle. In this paper, § 2 presents the numerical method, the flow configuration and parameter choices. Particle inertial effects on transition are presented in § 3. The modulation of the turbulence regeneration cycle is reported through modal analysis in § 4.

2. Simulation method and validation

2.1. *Numerical method*

Direct numerical simulations of single-phase flows are performed for an incompressible Newtonian fluid. A pseudospectral method is employed in the periodic directions (streamwise, x, and spanwise, z) and second-order finite differences are used for spatial discretization in wall-normal y direction. The solution is advanced in time by a third-order Runge–Kutta scheme. Incompressibility is achieved by correcting the pressure contribution, which is a solution of a Poisson equation. The fluid velocity and pressure fields are a solution of the continuity equation (2.1) and momentum balance equations (2.2) and (2.3):

$$\frac{\partial u_j}{\partial x_j} = 0, \tag{2.1}$$

$$\frac{\partial u_i}{\partial t} + u_j \frac{\partial u_i}{\partial x_j} = -\frac{1}{\rho_f}\frac{\partial p}{\partial x_i} + \nu \frac{\partial u_i}{\partial x_j \partial x_j} + \frac{1}{\rho_f} F_i, \tag{2.2}$$

$$F_i^k = -\sum_{k_s=1}^{8} \sum_{n=1}^{N_{k_s}} \frac{w_{k_s}^n}{\triangle V_{k_s}} f_i^n. \tag{2.3}$$

Using a projection technique, the body force in the momentum balance equation (2.3) accounts for the particle momentum contribution to node k of the fluid based on particles in all of the eight computational volumes (k_s) which share this node. Parameter $w_{k_s}^n$ is the linear geometric weight for each particle n based on its distance from node k, and the inner summation is over all N_{k_s} particles in the volume k_s.

Numerical simulations of particle trajectories and suspension flow dynamics are based on the standard Lagrangian point-particle approximation where the particle-to-fluid density ratio $r \equiv \rho_p/\rho_f \gg 1$ and the particle size is smaller than the smallest viscous dissipation scales of the turbulence. As a consequence of this and the low volume concentrations (a maximum volume fraction of $\overline{\Phi_V}$ less than 1×10^{-3} is used in this study), only the Stokes drag force and two-way coupling have been incorporated (see Balachandar & Eaton 2010). The velocity of particle n is governed in (2.4) and particle trajectories are then obtained from numerical integration of the equation of motion (2.5):

$$\frac{\mathrm{d}u_{p,i}^n}{\mathrm{d}t} = \frac{f_i^n}{m_p} = \frac{1}{\tau_p}[1 + 0.15(Re_p^n)^{0.687}](u_{f,i}^n - u_{p,i}^n), \tag{2.4}$$

$$\frac{\mathrm{d}x_i^n}{\mathrm{d}t} = u_{p,i}^n, \tag{2.5}$$

where $\tau_p = \rho_p {d_p}^2/18\mu$ is the Stokes relaxation time of the particle, m_p is the particle mass and the particle Reynolds number $Re_p^n = |u_{f,i}^n - u_{p,i}^n| d_p^n/\nu$ is based on the

magnitude of the particle slip velocity ($u^n_{f,i} - u^n_{p,i}$) and particle diameter d^n_p. In this work, the average Re^n_p is between 0.125 ($r = 80$, two-way) and 3.25 ($r = 8000$, one-way), which is far smaller than the suggested maximum $Re_p \approx 800$ for the Stokes drag correction in (2.4) (Schiller 1933). Thus the Re_p correction to the Stokes drag is minimal in this study. In order to highlight the effect of particle response time, we do not consider gravitational settling. Other terms in the particle momentum equation (see Maxey & Riley 1983) are neglected since they remain small compared with drag when the density ratio $r \gg 1$. These neglected terms are also found to have less effect on the stability analysis in relatively low-Reynolds-number turbulence as demonstrated by Klinkenberg, de Lange & Brandt (2014). Particle–particle collisions are not taken into consideration due to the low volume concentrations, and we exert a purely elastic collision between particles and the upper/lower walls. This purely elastic wall collision is commonly used in gas–solid turbulence (Li *et al.* 2001; Sardina *et al.* 2012; Zhao *et al.* 2013). However, we have tested the restitution coefficient $|u^n_{p,init}/u^n_{p,final}|$ between 0.5 and 1 and do not observe significant changes to particle distributions or two-way coupling, consistent with Li *et al.* (2001).

In addition to the point force approximation as implemented in (2.3), there are other techniques that can be used to account for two-way coupling in particle-laden flows. For example Pan & Banerjee (1996) use the pressure gradient and stress tensor from an analytic velocity disturbance field to replace the point force, Capecelatro & Desjardins (2013) use a volume filtering operator to replace the point sources by smoother, locally filtered fields and Gualtieri *et al.* (2015) present an exact regularized point particle method which includes the far-field disturbance by applying a multipole expansion to obtain the Stokeslet. In order to validate our current method, we compared both with the results of Zhao *et al.* (2013) at $Re_\tau = 180$ with $\tau^+_p = 30$ as well as with results from Capecelatro & Desjardins (2013) at $Re_\tau = 235$ with $\tau^+_p = 65$. The mean velocity profile, concentration profile and root mean square (RMS) velocity profile agree well with each other (not shown here), which suggests that the current particle in cell method for two-way coupling is suitable for our study, and is not sensitive to the two-way coupling scheme. Additional details and validation of the numerical scheme can be found in previous work for both one-way coupling and two-way coupling (Richter & Sullivan 2013; Sweet, Richter & Thain 2018).

2.2. *Single-phase PCF*

Simulation of PCF turbulence in the miniunit configuration is used in the rest of this paper, at a relatively low Reynolds number (just above the onset of transition to turbulence). The flow is driven by two walls moving at equal and opposite velocities, and by imposing a no-slip condition on each. Boundary conditions in the lateral, wall-parallel directions are periodic. The Reynolds number is defined using half of the relative wall velocity and half of the gap between the two walls. The turbulent state is obtained by inducing fluctuations into a laminar flow at a high Reynolds number and once a turbulent state is developed, the Reynolds number is decreased gradually to a desired Reynolds number. The grid used in this work is $N_x \times N_y \times N_z = 32 \times 64 \times 32$ (grid convergence tests (not shown here) have ensured that results are independent of grid resolution) corresponding to a resolution in wall units of $\Delta x^+ \times \Delta y^+$(wall, centre) $\times \Delta z^+ \approx 6.8 \times (1, 1.5) \times 4.7$. Figure 2 shows the mean velocity profile and velocity fluctuations in all three directions, in comparison with Wang *et al.* (2017) who used a second-order centred finite volume method and Kawahara & Kida (2001) who used a pseudospectral discretization in all three directions. We can see that the RMS velocity

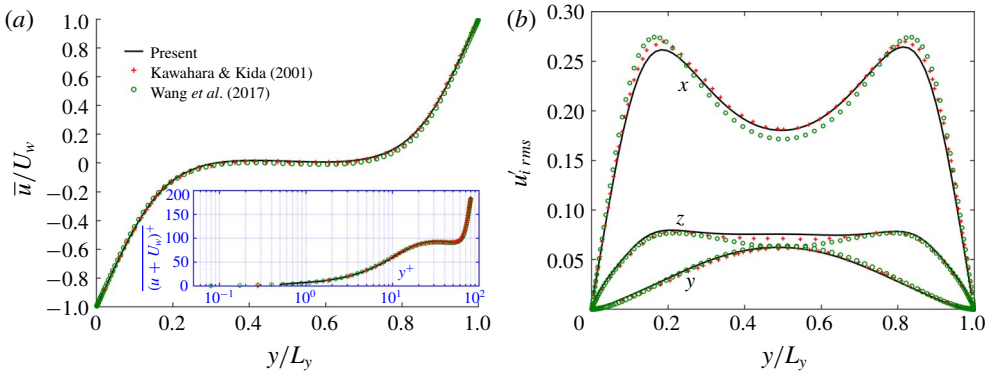

FIGURE 2. (Colour online) Comparison between current study and published data from Kawahara & Kida (2001) and Wang, Abbas & Climent (2017) in single-phase flow at $Re_b = 400$: (*a*) mean velocity profiles; (*b*) fluctuation velocity RMS in three directions.

fluctuations from the present simulations agree well with Kawahara & Kida (2001), whereas there is a small discrepancy between the current work and Wang *et al.* (2017) in the streamwise and spanwise directions near the centre region. This might be due to the slight difference of domain size in the spanwise direction which confines the shape of two counter-rotating rolls in miniunit.

2.3. *Suspension flow configurations*

Table 1 contains several selected parameters for the statistical and modal analysis in this study (i.e. the cases used for all analyses but not including the transition tests of § 3.1). The case number indicates the bulk Reynolds number, density ratio and particle volumetric concentration used in that particular simulation. Turbulence–laminar transition occurs near case 380–900–4. Hamilton & Abernathy (1994) found a minimum threshold of streamwise vorticity circulation of the LSVs (below which the transition happens), and therefore we use this case to check if this threshold is modified by the presence of inertial particles.

The Kolmogorov scale is difficult to determine and somewhat ambiguous at the low turbulence levels in these simulations, although we can estimate that the minimum dissipation scale is about 1.5 times the viscous length scale at the wall, which itself is about 2.0 times the viscous length scale in the centre (Pope 2000). The ratio of the particle to fluid time scale defines the Stokes number $St_{turb} \equiv \tau_p/\tau_f$, where $\tau_f \equiv L_y/\max(v'|w')$ is related to the turnover time scale of the LSVs (Massot 2007; Wang *et al.* 2017). The estimation of τ_f is about 25 time units (time unit defined as h/U_w) from figure 7(*a*). In the context of high-Reynolds-number atmospheric boundary layer flows, the particle Stokes number τ_p^+ based on the viscous scale corresponds to a diameter of $d \approx 30$ μm to $d \approx 90$ μm at $Re_\tau \approx 10^4$ within 1 m of the surface when the particle density is of the order of 1000 kg m^{-3}. In order to gain insight into the finite-size effects on particle dispersion and turbulence modulation, we specifically select one group of parameters τ_p^+ and St_{turb} to be nearly the same as the finite-size particles used in Wang *et al.* (2017). There are two cases, 500–5000–4 and 500–8000–4, with extremely high density ratios that are intended to help build a complete understanding of the effect of Stokes number on particle dispersion in the LSVs in our model flow. These high density ratios are simulated with one-way coupling only since they fully laminarize the flow at $Re_b = 500$.

Miniunit in plane Couette flow
$L_y/d = 80$; $L_x \times L_y \times L_z = 2.75 \times 1.0 \times 1.88$
$N_x \times N_y \times N_z = 32 \times 64 \times 32$
$\Delta x^+ \times \Delta y^+$(wall, centre) $\times \Delta z^+ = 6.8 \times (1.0, 1.5) \times 4.7$

Case (Re_b–r–$\overline{\Phi_v}$)	r (ρ_p/ρ_f)	$\overline{\Phi_m}$	u_τ ($\times 10^{-2}$)	δ_v ($\times 10^{-2}$)	Re_τ	L_y^+	d^+	τ_p^+	St_{turb}	Couple
500–0–0	—	—	4	1.25	40	80	—	—	—	—
Finite size	5	0.1	4.1	1.25	40	80	4	4.44	0.056	FCM
500–80–4	80	0.032	4.1	1.23	40.6	81.2	1.01	4.58	0.056	2-way
500–80–10	80	0.08	4.1	1.23	40.6	81.2	1.01	4.58	0.056	2-way
500–500–4	500	0.1	4.1	1.21	41.2	82.5	1.03	29.5	0.347	2-way
500–900–4	900	0.36	4.1	1.23	40.6	81.2	1.02	51.6	0.625	2-way
380–900–4	900	0.36	4.6	1.09	36.7	73.4	0.92	41.9	0.499	2-way
500–5000–4	5000	2.0	4.1	1.25	40	80	1.01	278	3.47	1-way
500–8000–4	8000	3.2	4.1	1.25	40	80	1.01	444	5.56	1-way

TABLE 1. Parameters of baseline numerical simulations. The Reynolds number $Re_b \equiv U_w h/\nu$, where U_w is half of the relative velocity and $h = L_y/2$ is half of the gap between two walls. The friction Reynolds number is $Re_\tau \equiv u_\tau h/\nu$ and the particle Stokes relaxation time is $\tau_p \equiv \rho_p d^2/(18\rho_f \nu)$, where d represents the particle diameter. The superscript '+' is the dimensionless number based on viscous scale, where δ_v, u_τ and ν/u_τ^2 correspond to the viscous length scale, velocity scale and time scale, respectively. FCM (force coupling method) is a low-order multipole expansion for capturing finite-size effects used by Wang *et al.* (2017).

3. Effect of inertial particle response time

3.1. *Effects of particle response time and mass loading on transition*

While linear stability analysis is a key tool in understanding the effects of a dispersed phase on transition, it often must assume that the flow is uniformly (or with some other specified distribution) laden with particles, and that the flow is two-dimensional (Saffman 1962; Michael 1964; Dimas & Kiger 1998; Rudyak, Isakov & Bord 1998). Clearly, this type of analysis is fundamentally limited in uncovering nonlinear effects such as the regeneration cycle or inertial accumulation of particles (Squires & Eaton 1990; Eaton & Fessler 1994), and theoretical predictions are difficult to develop. The interactions of inertial particles with coherent structures (e.g. LSSs and LSVs in PCF; see figure 6*a*) complicate matters and necessitate a fully nonlinear analysis. For this reason we examine the turbulent-to-laminar transition threshold from an empirical point of view, by simulating a fully developed turbulent PCF experiencing (i) successive reduction of the Reynolds number for several density ratios (figure 3*a*,*b*), (ii) successive increase of the particle density at a fixed Reynolds number (figure 3*c*) and (iii) successive increase of the particle mass loading for several density ratios at a fixed Reynolds number (figure 3*d*). Identifying a rigorous turbulent–laminar transition threshold would require a large number of simulations to form converged relaminarization statistics. Instead of pinpointing this value, we are instead interested in classifying the particle influence as either stabilizing or destabilizing and examining the impact of the particles on flow features, and therefore do not attempt to specify the true critical Reynolds numbers.

Transition of single-phase flow is observed at $Re_c \sim 320$ which is nearly the same as in Wang *et al.* (2018) in the miniunit domain. The wall friction coefficient

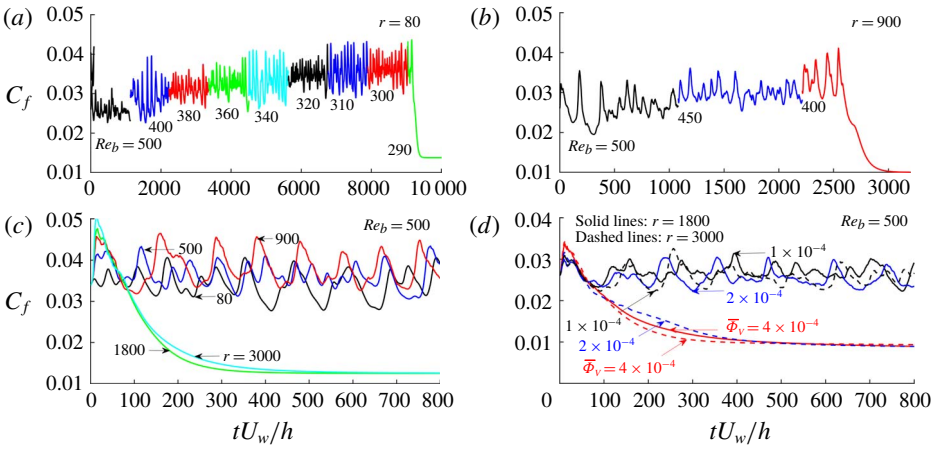

FIGURE 3. (Colour online) Effect of inertial particles on the turbulence-to-laminar transition as indicated by the temporal evolution of C_f. This is demonstrated by gradually decreasing Re_b, density ratio (r) and bulk volumetric concentration ($\overline{\Phi_V}$) starting from a fully turbulent simulation at $Re_b = 500$. (*a*) Case 500–80–4, decreasing $Re_b = 500$ to $Re_b = 290$; (*b*) case 500–900–4, decreasing $Re_b = 500$ to $Re_b = 400$; (*c*) fixed $Re_b = 500$ and increasing density ratio $r = 80$ to $r = 3000$; (*d*) fixed $Re_b = 500$ and two density ratios $r = 1800$ and $r = 3000$, Φ_b decreasing from 4×10^{-4} to 1×10^{-4}.

$C_f = 2\overline{\tau}_w/(\rho U_w^2)$ (summed on both walls) is used as an indicator of current flow regime. The same initial turbulent flow configurations were chosen from the single-phase flow simulations at $Re_b = 500$ for all tests. The particles were then randomly seeded in the simulation domain. The two-phase flow simulations were integrated for at least 1200 time units (h/U_w) before the Reynolds number was abruptly decreased, in order to accurately evaluate the transition threshold. The evolution in time of the wall friction coefficient is shown in figure 3 for the various tests. Figure 3(*a*,*b*) shows the successive reductions of the Reynolds number down to turbulent-to-laminar transition for $r = 80$ ($Re_c \sim 290$) and $r = 900$ ($Re_c \sim 400$) with the same volumetric concentration of $\overline{\Phi_V} = 4 \times 10^{-4}$. We also perform similar tests (not shown in this figure) for $r = 200$ ($Re_c \sim 240$), $r = 300$ ($Re_c \sim 260$) and $r = 500$ ($Re_c \sim 310$). Figure 3(*c*) shows the successive increase of the particle density up to the turbulence-to-laminar transition for $Re_b = 500$ (transition occurs between $r = 900$ and $r = 1800$) with the same volumetric concentration of $\overline{\Phi_V} = 4 \times 10^{-4}$. Finally, figure 3(*d*) shows the successive increase of the particle volume/mass loading for two density ratios $r = 1800$ (transition occurs by $\overline{\Phi_V} = 4 \times 10^{-4}$) and $r = 3000$ (transition occurs by $\overline{\Phi_V} = 2 \times 10^{-4}$).

Clearly, two limiting cases exist: at small density ratios (thus small Stokes numbers since d_p is held constant) the flow experiences destabilization and the critical Reynolds number is lowered, and at high density ratios (high Stokes numbers) the particles tend to stabilize the turbulence and increase the critical Reynolds number. This is consistent with the linear stability prediction given by Saffman (1962). For particles with high density ratios, the damping effect on turbulence varies monotonically with mass loading (again consistent with previous studies (Saffman 1962; Dimas & Kiger 1998; DeSpirito & Wang 2001)), at least in the dilute regimes considered here. The turbulence attenuation effect is enhanced with an increased particle mass loading as

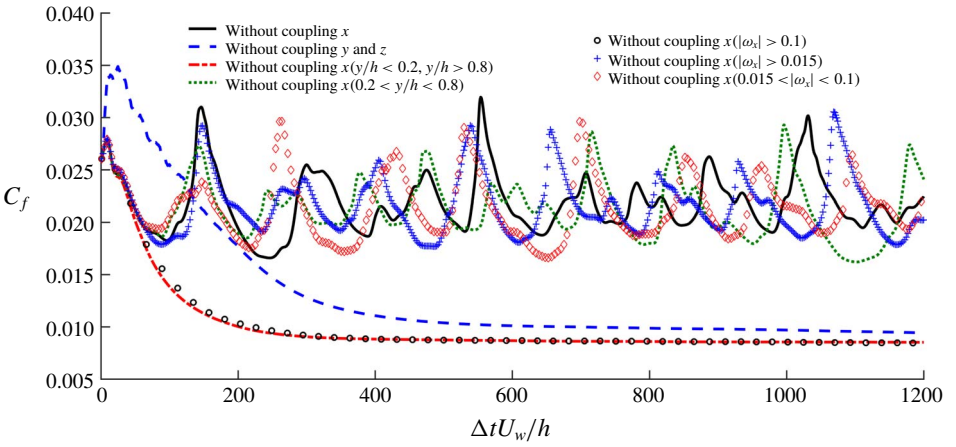

FIGURE 4. (Colour online) Turbulence–laminar transition threshold indicated by the temporal evolution of C_f. A 'conditional' test of sensitivity due to inertial particle drag force applied in different spatial regions in case 500–3000–4.

seen in figure 3(*d*). In pressure-driven flow, Klinkenberg *et al.* (2011) proposed a modified Reynolds number ($Re_m = (1 + \overline{\Phi_m})Re_b$) for heavy particles via analysis of the standard Orr–Sommerfeld–Squire system. This effective Reynolds number can only predict turbulence damping (and an increase of the critical Reynolds number) and has a proportional increase with the particle mass loading. Comparing this estimate based on Re_m to the present simulations, we obtain

$Re_c \sim 400$–450 for $r = 900$ and $\overline{\Phi_V} = 4 \times 10^{-4}$ (predicted $Re_m = 435$);
$Re_c \sim 500$ for $r = 900$ to 1800 and $\overline{\Phi_V} = 4 \times 10^{-4}$ (predicted $Re_m = 435$–550);
$Re_c \sim 500$ for $r = 1800$ and $\overline{\Phi_V} = 2 \times 10^{-4}$ to 4×10^{-4} (predicted $Re_m = 435$–550);
$Re_c \sim 500$ for $r = 3000$ and $\overline{\Phi_V} = 1 \times 10^{-4}$ to 2×10^{-4} (predicted $Re_m = 416$–512).

We therefore find that the transition Reynolds number found in the PCF laden with high-inertia particles ($St_{turb} > 0.5$, where turbulence is attenuated) is in the range of the estimates using the modified Reynolds number predicted by Klinkenberg *et al.* (2011).

3.2. *Conditional test of two-way coupling*

For pointwise particles, two-way coupling is realized by applying a corrected three-dimensional Stokes drag with Navier–Stokes equation as in (2.4). The extra dissipation (the loss of kinetic energy due to fluid–particle interactions; see Zhao *et al.* (2013)) plays the key role in providing a stabilizing effect. In order to further investigate the key coupling components that lead to stabilization and turbulence attenuation, we perform a 'conditional' test in this section.

As shown in figure 4, we begin with the case 500–3000–4 (initialized from an unladen turbulent flow field at $Re_b = 500$) with randomly distributed particles. The flow decays into laminar flow with normal, full two-way coupling. By artificially removing the interphase coupling force in either the streamwise x direction or both the y and z directions throughout the whole domain, we first find that streamwise coupling is the primary mechanism that attenuates the turbulence (i.e. without y and z coupling the flow still transitions from turbulent to laminar). From here, the streamwise coupling is only removed (i) from the spatial region where the regeneration cycle is active ($0.2 < y/h < 0.8$) or (ii) from the inactive region ($y/h < 0.2$ and $y/h < 0.8$).

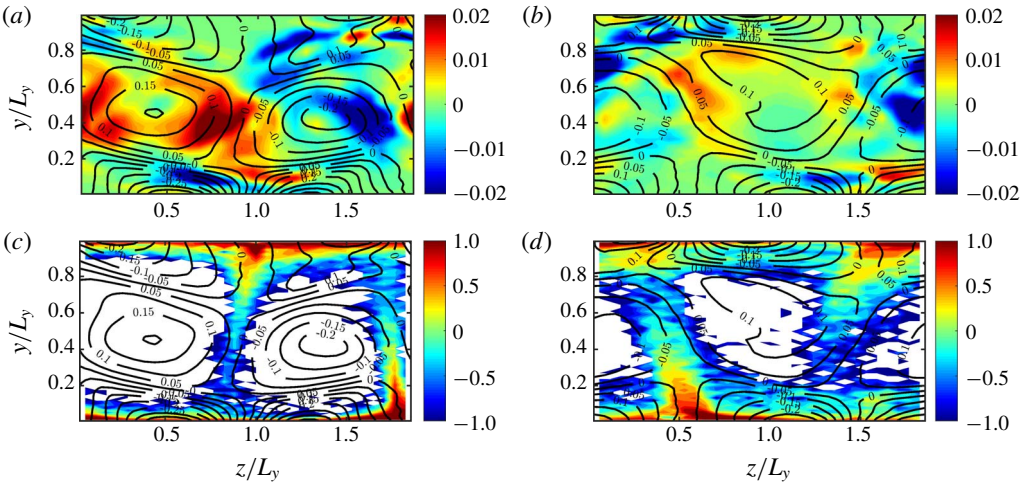

FIGURE 5. (Colour online) (*a*,*b*) Contour of temporal average of streamwise vortex stretching term in one single cross-section (y, z plane) within 50 time units and isolines of temporal and streamwise average of streamwise vorticity within 50 time units. (*c*,*d*) Contour (logarithmic scale) of temporal and streamwise average of normalized concentration by the bulk value and isolines of temporal and streamwise average of streamwise vorticity within 50 time units. (*a*,*c*) Case 500–500–4; (*b*,*d*): case 500–900–4.

Turbulence is sustained by removing streamwise coupling in the region associated with the regeneration cycle, suggesting that it is streamwise coupling in this region that is responsible for laminarization. Further, we remove the streamwise coupling in different radial positions relative to the LSVs (strong streamwise vorticity $|\omega_x| > 0.1$ is in the central region of the LSVs, $|\omega_x| > 0.015$ is a larger region containing $|\omega_x| > 0.1$ and $0.015 < |\omega_x| < 0.1$ is an annulus formed by subtracting the area $|\omega_x| > 0.1$ from $|\omega_x| > 0.015$). This analysis, shown in figure 4 as red diamonds, demonstrates that streamwise coupling, specifically in the region associated with the annulus given by $0.015 < |\omega_x| < 0.1$ and in the region associated with the regeneration cycle, should be considered as the most sensitive region which might be altered by the inertial particles, leading to turbulence attenuation.

To visualize this stabilization process that occurs in the annulus of region $0.015 < |\omega_x| < 0.1$, figure 5(*a*,*b*) shows the contour of streamwise vorticity stretching $\omega_x \partial u/\partial x$. This is a streamwise-dependent quantity, so we time-average (50 time units) at a single cross-section at $x = L_x/2$. Figure 5(*c*,*d*) shows the contour of the normalized particle concentration with respect to the bulk concentration at the same location and averaged over the same time. The isolines in all panels are the streamwise-averaged streamwise vorticity ($\overline{\omega_x}(y, z)$). Figure 5(*a*,*c*) and figure 5(*b*,*d*) show cases 500–500–4 and 500–900–4, respectively. It is clear that strong vorticity stretching happens in the range of $0.015 < |\omega_x| < 0.1$, which is a key component of the self-sustaining regeneration cycle. The intensity of this stretching is reduced in case 500–900–4 (contour in figure 5*b*) compared to that of case 500–500–4 (contour in figure 5*a*). Simultaneously, we find that there are more particles present in the range of $0.015 < |\omega_x| < 0.1$ in case 500–900–4 (figure 5*d*) than in case 500–500–4 (figure 5*c*).

As a result, we associate the turbulence attenuation with the streamwise coupling of high-inertia particles (e.g. $St_{turb} = 0.625$), and their presence in the range of

$0.015 < |\omega_x| < 0.1$ is of key significance since this is the region which has the strongest streamwise vortex stretching effect. Below, we argue that the streamwise vortex stretching and the LSVs are the key sub-steps in the regeneration cycle, and coupled to each other. The preferential presence of particles in this streamwise vortex stretching region is an important phenomenon which alters the regeneration cycle and thus the transition from turbulent to laminar flow, and has been observed at higher Reynolds numbers (Lee & Lee 2015).

3.3. *Particle distribution and velocity profile*

For inertial pointwise particles, their spatial distribution is determined through the drag force exerted from large-scale turbulent structures to the particles. Due to inertia, heavy particles tend to be expelled from the vortex centre to the low-vorticity but high-strain-rate regions (Druzhinin & Elghobashi 1998). As argued above, this process plays a key role in turbulence modulation since particles tend to accumulate in regions associated with streamwise vortex stretching. In a similar study focused on neutrally buoyant finite-sized particles, Wang *et al.* (2018) found that particles accumulating in the streaks tend to enhance the turbulence whereas particles accumulating in the large-scale rolls hardly modify turbulence levels.

Figure 6(*a*) shows an instantaneous particle distribution over a (y, z) cross-sectional plane with different density ratios ($r = 80$–8000) at the same Reynolds number ($Re_b = 500$) and volumetric concentration ($\overline{\Phi_v} = 4 \times 10^{-4}$) at a point in time corresponding to the strongest LSSs during the regeneration cycle. From left to right, top to bottom, it is clear that particles with low to moderate inertia tend to accumulate in the LSSs whereas particles with a higher inertia distribute more homogeneously and spread throughout the Couette gap, a behaviour seen in other particle-laden, wall-bounded turbulent flows. Along the same lines, particles with density ratio from $r = 300$ to 500 are mostly trapped inside the LSSs, even during the streak breakdown process (not shown). Either lower (e.g. $r = 80$) or higher (e.g. $r = 900$) than this density ratio, the particles can stray from the LSS regions, consistent with known behaviour of inertial particles (Maxey 1987; Druzhinin & Elghobashi 1998). In a Taylor–Green vortex (TGV) set-up, Massot (2007) proposed a threshold of the ratio between particle response time and the TGV turnover time scale. Below the threshold, particles will stay inside this cell whereas particles tend to move to the other cells above the value. We numerically obtained the single-particle trajectory in TGV flow with the same particle time scale corresponding to particles in the present simulated turbulent LSVs. The particle behaviour in TGV flow is analogous to particle distribution in turbulent PCF with the same particle time scale (data are not shown here). Case 500–80–4 has a low $St_{turb} \approx 0.056$ causing the particles to behave more as tracers and stay in one LSV, whereas case 500–8000–4(1way) with a high $St_{turb} \approx 5.56$ leads to particles which cannot follow the streamlines and cross the LSVs after being ejected by ejection events. Particles with intermediate Stokes numbers, as in case 500–500–4 with $St_{turb} \approx 0.35$, are expelled from the LSVs and become trapped inside the LSSs.

This non-monotonic change in particle distribution can be seen in figure 6(*b*), where the normalized particle volume concentration is shown. With increasing density ratio from 500–80–4 to 500–300–4, the concentration decreases in the centre whereas it increases in the near-wall region. We observe an opposite tendency when further increasing the density ratio from 500–300–4 to 500–1200–4. At higher density ratios with two-way coupling, transition to laminar flow occurs in the present simulations.

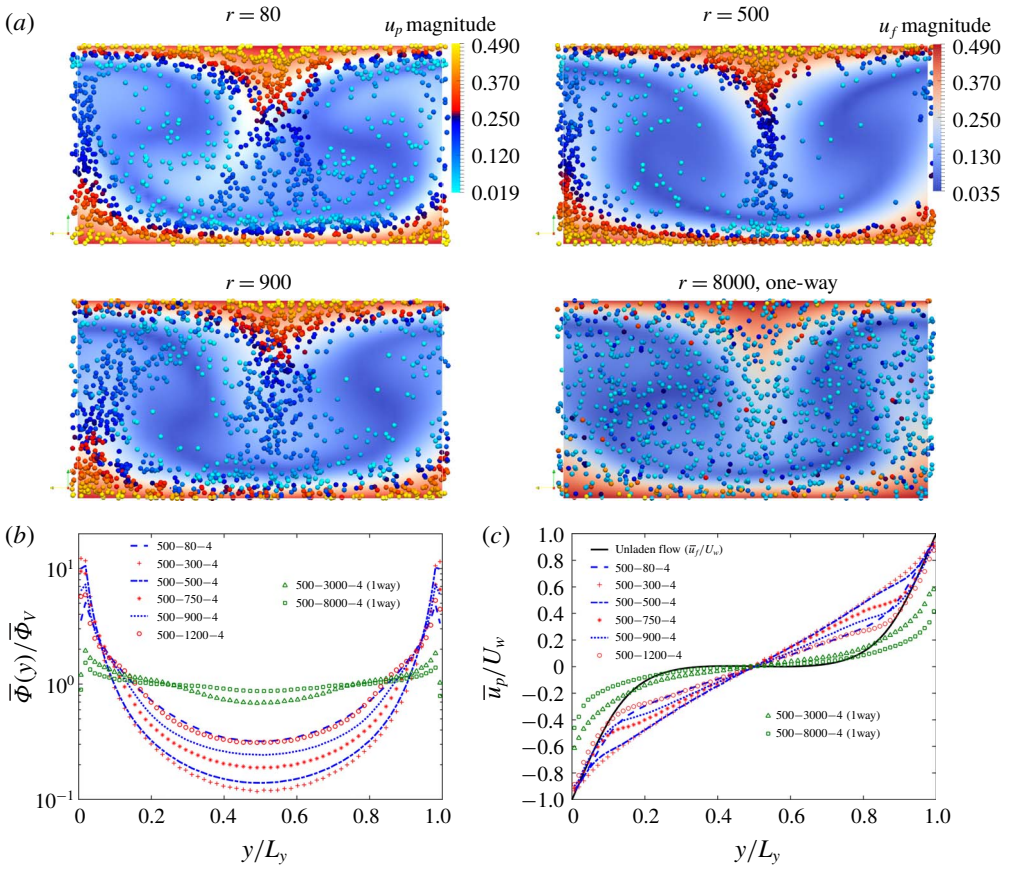

FIGURE 6. (Colour online) (*a*) Contours of the magnitude of the streamwise flow velocity (colourbar in upper left panel) and instantaneous particle positions projected onto the (y, z) cross-section when the LSS is strongest before breakdown, coloured according to magnitude of particle streamwise velocity (colourbar in upper right panel). The particle size shown in the panels is magnified four times for better visualization. Top-left: case 500–80–4; top-right: case 500–500–4; bottom-left: case 500–900–4; bottom-right: case 500–8000–4 (one-way coupling). (*b*) Mean volume concentration normalized by the bulk concentration. (*c*) Mean streamwise velocity scaled by U_w.

At higher flow Reynolds number ($Re_b = 2025$), the increase of particle concentrations in the centre with increasing particle response time ($\tau_p^+ \approx 90$ corresponding to $St_{turb} \approx 1.06$) is also observed by Richter & Sullivan (2013). For the sake of highlighting the long particle response time effect on the particle distribution, we also show cases 500–3000–4 and 500–8000–4 with one-way coupling, where we can find a nearly homogeneous concentration profile because particles cannot follow the streamlines.

Despite the slip velocity between the particulate phase and fluid phase, the shape of the mean particle velocity profile is mainly determined by the carrier phase. In particular, the mean particle streamwise velocity will reflect the local mean fluid velocity profile of the structure it is contained within (e.g. LSSs or LSVs). Hamilton *et al.* (1995) have shown that for the miniunit configuration, the characteristic 'S'

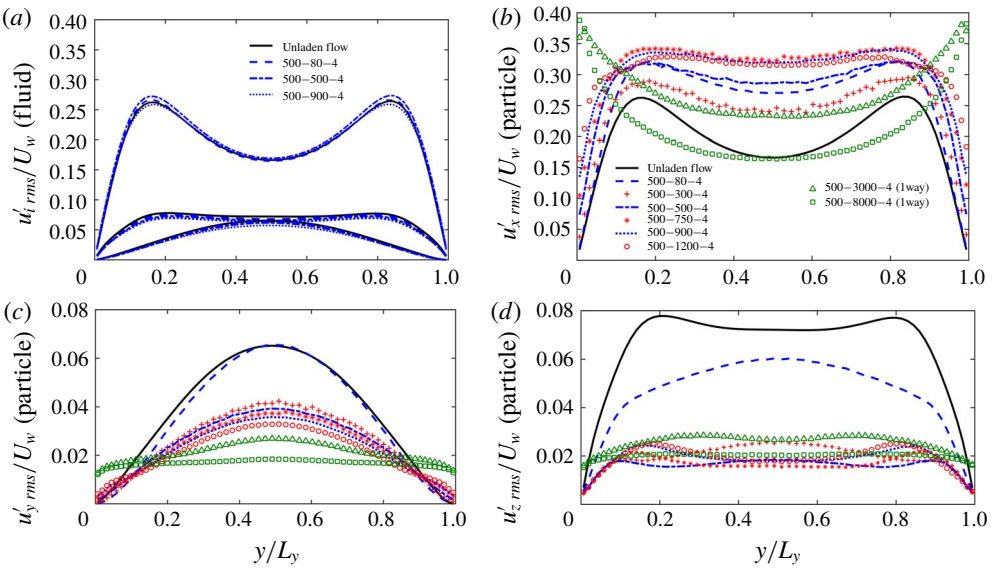

FIGURE 7. (Colour online) RMS velocity fluctuations in cases with density ratios. (*a*) Fluid phase in three directions. (*b–d*) Particulate phase in three directions: (*b*) streamwise direction fluctuation; (*c*) wall-normal direction fluctuation; (*d*) spanwise direction fluctuation. In (*b–d*), fluid phase in single phase is plotted as a reference.

shape of the mean velocity profile in PCF is governed primarily by the LSVs in single-phase flow. Figure 6(*c*) compares the mean fluid velocity (solid black line) to the mean particle velocities $\overline{u_p}/U_w$ of particles with varying density. There is a clear distinction between the nearly linear (respectively 'S') shape of the mean particle velocity curve for 500–300–4 (respectively 500–3000–4(1way)) if the particles are trapped in the LSSs (respectively across the whole domain). Again, this effect is non-monotonic with particle inertia. For cases 500–3000–4(1way) and 500–8000–4(1way), the qualitative shape of the mean particle velocity is similar to that of mean fluid velocity in single-phase flow; this discrepancy is due to the difference between the particle response time scale and the turnover time of the LSV.

3.4. *Turbulence intensity*

The RMS velocity fluctuations for the various cases are plotted in figure 7. Figure 7(*a*) shows the RMS velocities in all three directions for the fluid phase, where it is apparent that $u'_{f\,rms}$ is nearly unchanged whereas in the core region $v'_{f\,rms}$ and $w'_{f\,rms}$ decrease slightly with increased particle inertia. The particulate RMS velocity fluctuations are shown in figure 7(*b–d*); the single-phase velocity fluctuations are also plotted as a reference (solid black lines). As noted by Yu, Vinkovic & Buffat (2016), particles moving away from the wall are associated mainly with ejections while particles moving towards the wall are associated with sweeps. As seen above, inertial particles with low to moderate Stokes numbers tend to remain in the high-strain-rate region (see figure 6) – regions associated with high $u'_{f\,rms}$. This results in high values of $u'_{p\,rms}$ across the whole Couette flow gap which can be seen in figure 7(*b*). Thus the increase of particulate streamwise turbulent kinetic energy compared with single-phase flow is due to the accumulation of particles in the LSS which contains high streamwise turbulent kinetic energy.

The effect is opposite for $v'_{p\,rms}$ and $w'_{p\,rms}$. The fluid velocity fluctuations $v'_{f\,rms}$ and $w'_{f\,rms}$ are high in the outer regions of the LSVs (not shown here). Therefore when the inertial particles collect in high-strain-rate regions (intermediate Stokes numbers), their spanwise and wall-normal velocity fluctuations are much smaller than the fluid average. At low Stokes numbers, long residence times in the LSVs allow particles to gain wall-normal and spanwise kinetic energy (figure 7*c*,*d*). At high Stokes number, particles tend to again distribute homogeneously throughout the whole domain. Particles move across LSVs, but their inability to quickly adjust their velocity results in suppressed values of $v'_{p\,rms}$ and $w'_{p\,rms}$.

As a final note, we have compared the particle distribution, mean velocity and RMS velocity fluctuations (not shown here) between case 500–80–4 and a simulation with finite-size particles from Wang *et al.* (2017); both have the same particle response time. We find that even for the same Stokes number, finite-size particles collect more in the central region and that their mean velocity and fluctuations are similar to the fluid phase. This difference is due directly to finite-size effects which should be considered for physical systems where particle diameters are larger than the dissipation scales of the flow.

4. Modal analysis of the regeneration cycle modulation

Turbulence regeneration mechanisms in wall turbulence involve three-dimensional, multiscale structures, and the relevant nonlinear dynamics involved is neglected when performing linear stability analyses on laminar-to-turbulent transition and streak stability. Therefore to leverage the present nonlinear simulations, modal analysis is used to determine the natural mode shapes and frequencies in this miniunit PCF system – this strategy significantly simplifies the range of temporal and length scales in the turbulent flow, thereby highlighting the essential features (e.g. LSSs and LSVs) in the regeneration cycle. To start, it is helpful to provide a list of relevant quantities which are useful in defining the various stages/structures of the regeneration cycle, which will be further analysed in this section.

(i) The turbulent kinetic energy contained in the streaks and its corresponding Fourier modes yield information about the contributions from various scales in the flow. We define $\mathcal{M}(k_x = m\alpha,\, k_z = n\beta)$ as the vertically integrated modal RMS velocity modes in the two periodic directions (x and z), following Hamilton *et al.* (1995):

$$\mathcal{M}(m\alpha,\, n\beta) \equiv \left\{ \int_0^{L_y} [\widehat{u'}^2(m\alpha,\, y,\, n\beta) + \widehat{v'}^2(m\alpha,\, y,\, n\beta) + \widehat{w'}^2(m\alpha,\, y,\, n\beta)]\, \mathrm{d}y \right\}^{1/2}, \quad (4.1)$$

where $(\alpha,\ \beta)$ are the fundamental wavenumbers in the streamwise and spanwise directions (defined as $(2\pi/L_x,\, 2\pi/L_z)$), and m and n are integers. In principle, each mode $(m\alpha, n\beta)$ provides information about specific structures in the flow. For instance in the miniunit domain (note that this may not necessarily be true in full domains):

$\mathcal{M}(0, \beta)$ represents the LSSs since it is the zeroth mode in the streamwise direction, and any mode $(0, n\beta)$ with $n \neq 0$ is an x-independent structure;

$\mathcal{M}(\alpha,\, 0)$ represents meandering streaks where the other $\mathcal{M}(m\alpha,\, n\beta)$ with $n \neq 0$ modes are very weak.

(ii) Circulation represents the intensity of the LSVs in the miniunit. Hamilton & Abernathy (1994) and Hamilton *et al.* (1995) stipulated that over one cycle, vortices must have a maximum circulation above a given threshold in order to produce an LSS through the lift-up process. Thus this integrated quantity provides a good measure

of whether or not this essential process can occur. The circulation of the streamwise vortices of mode zero in the streamwise direction (x-independent) and mode $n \neq 0$ in the z direction (z-dependent) is given by

$$\mathcal{C}(0, n\beta) \equiv \int_0^{L_y} \hat{\omega}_x(0, y, n\beta)\, \mathrm{d}\boldsymbol{S}(\boldsymbol{n}), \tag{4.2}$$

where $\boldsymbol{S}(\boldsymbol{n}) \equiv \mathrm{d}y \cdot L_z/n$ is the transverse surface with y varying from 0 to L_y and z varying from 0 to $2\pi/(n\beta)$ for $n \neq 0$. Based on our calculations, the maximum circulation in the miniunit domain always corresponds to $n = 1$, and therefore we define circulation as $\mathcal{C}(0, \beta)$ and use this measure to stand for the intensity of LSVs.
(iii) Lift-up: in the buffer layer, elongated streaks form on both sides of an LSV (see figure 6*a*). The so-called lift-up effect has been identified as a very robust mechanism for the generation of streaky motions in both transitional and turbulent flows (Ellingsen & Palm 1975; Hamilton *et al.* 1995; Brandt 2014). Fluid in the near-wall region is lifted away from the wall by the longitudinal vortical structures into a region of higher-speed fluid (so-called ejection), producing a low-speed streak. Simultaneously on the other side of the vortex, high-speed fluid is pushed towards the wall (so-called sweep), creating a high-speed streak. Consequently in shear flows, the main linear mechanism for transient disturbance growth is the lift-up effect that produces low- and high-speed streaks in the streamwise velocity (Ellingsen & Palm 1975). Bech *et al.* (1995) stated that the inner shear layer is formed via the lift-up of low-speed streaks from the viscous sub-layer. Once this occurs, the shear layers are coupled to an instantaneous velocity profile with an inflectional character, and they have been observed to become unstable and break up into chaotic motion, so-called 'bursting'. Specifically in Fourier space, Hamilton *et al.* (1995) have shown that the term most responsible for extracting energy from the mean shear flow is given by

$$\mathcal{L}(0, n\beta) \equiv \int_0^{L_y} \widehat{v'}(0, y, n\beta) \frac{\partial U(y)}{\partial y}\, \mathrm{d}y, \tag{4.3}$$

where $\widehat{v'}$ is the wall-normal fluctuation velocity in Fourier space and $\partial U(y)/\partial y$ is the gradient of the mean steamwise velocity.
(iv) Steamwise vortex stretching: during streak breakdown, nonlinear interactions reinforce the streamwise LSVs, leading to the formation of a new set of streaks, and completing the regeneration cycle. Hamilton *et al.* (1995) proposed that the strengthening of the vortices is due to interactions among the α-modes, which grow during the streak breakdown. Schoppa & Hussain (2002) suggested that the vortex formation is inherently three-dimensional, with direct stretching (inherent to streak (x, z)-waviness) of near-wall ω_x sheets leading to streamwise vortex collapse. They provided insights into the dynamics of near-wall vortex formation through the inviscid equation for streamwise vorticity:

$$\frac{\partial \omega_x}{\partial t} = \underbrace{-u\frac{\partial \omega_x}{\partial x} - v\frac{\partial \omega_x}{\partial y} - w\frac{\partial \omega_x}{\partial z}}_{\text{advection}} + \underbrace{\omega_x \frac{\partial u}{\partial x}}_{\text{stretching}} + \underbrace{\frac{\partial v}{\partial x}\frac{\partial u}{\partial z} - \frac{\partial w}{\partial x}\frac{\partial u}{\partial y}}_{\text{tilting}} + \underbrace{\frac{\partial F_z}{\partial y} - \frac{\partial F_y}{\partial z}}_{\text{particle feedback}}. \tag{4.4}$$

In fully developed turbulent single-phase flow, the greatest contribution, in magnitude, to the temporal evolution of the vorticity $\partial \omega_x/\partial t$ is related to the tilting term (Sendstad & Moin 1992). However, Schoppa & Hussain (2002) have shown

that this term mainly contributes to the thin tail of the near-wall ω_x layer, and is not responsible for x-independent streamwise vortex formation ($(0,\beta)$ mode in the miniunit). In particle suspension flow, an additional term named particle feedback is added in the streamwise vorticity equation representing the contribution from the inhomogeneous distribution of the feedback force from the particles to the fluid. In appendix A, we do the comparison between the contributions to LSVs with $(0,\beta)$ from the stretching term and the particle feedback term within $20 < y^+ < 60$ where the regeneration cycle happens. The contribution from the particle feedback term to the LSV formation is much less than the contribution from the stretching term (about 10 % in case 500–80–4 and 17 % in case 500–900–4). Instead, vortex formation is dominated by stretching of streamwise vorticity. The local ω_x stretching is sustained in time and is mainly responsible for the vortex collapse, whose location coincides with the $+\omega_x\partial u/\partial x$ peak. The meandering of streaks provides the generation of $\partial u/\partial x$, and then direct stretching of positive and negative ω_x occurs in regions where $\partial u/\partial x$ is generated across the wavy streak flanks during the streak breakdown process. The stretching term is active only during the peaks of the cycle when local three-dimensionality is induced after streak breakdown (see Jiménez & Moin 1991). In Fourier space, the stretching term can be written as

$$\mathcal{S}(m\alpha, n\beta) \equiv \int_0^{L_y} \widehat{\omega}_x(p\alpha, y, q\beta)\frac{\partial \widehat{u}(r\alpha, y, s\beta)}{\partial x}\,\mathrm{d}y, \tag{4.5}$$

where the total time rate of change of streamwise vorticity in the $(m\alpha, y, n\beta)$ mode is the summation of terms over all values of p, q, r, s such that $p + r = m$ and $q + s = n$. The contribution to the LSV with $(0,\beta)$ comes from wavenumber combinations which satisfy $p + r = 0$ and $q + s = 1$. For the streamwise direction, Hamilton *et al.* (1995) demonstrated that $p = \pm 1$ and $r = \mp 1$ are the dominant terms producing additional streamwise vorticity in the right places where the higher x-wavenumber modes are negligible. It is difficult, however, to specify a single pair of modes combining both x-wavenumber and z-wavenumber which are dominant.

Therefore, we consider all pairs $p = \pm 1$ and $r = \mp 1$ satisfying the condition $m = p + r = 0$ in the streamwise direction and $q = -2$ to 3 and $s = 3$ to -2 satisfying the condition $n = q + s = 1$ in the spanwise direction (a total 12 pairs of x and z wavenumbers). A discrete Fourier transform can be expressed as a complex number containing the modulus and argument, and in appendix B we show the modulus of each of the 12 pairs of wavenumbers and their phase differences with the meandering streak. Since the summation of these 12 pairs as shown in figure 13 reflects around 91 % of the summation of all modes, we use this summation as a measure of the streamwise vortex stretching effect.

4.1. *Intensity of the characteristic terms of regeneration cycle*

Figure 8 shows the temporal evolution of the quantities defined in the previous section: the wall-normal integrated amplitude of LSSs ($\mathcal{M}(0,\beta)$; figure 8*a*), the strength of the meandering streak (represented by mode $\mathcal{M}(\alpha, 0)$; figure 8*a*), LSV strength (represented by $\mathcal{C}(0,\beta)$; figure 8*b*), the vortex stretching term (represented by $\mathcal{S}(0,\beta)$ which is the summation of all 12 pairs of $p = \pm 1$ and $r = \mp 1$ in combination with $q = -2$ to 3 and $s = 3$ to -2; figure 8*c*) and the lift-up term (represented by $\mathcal{L}(0,\beta)$ mode; figure 8*d*). Clearly, all of the signals are fluctuating in time with a similar period corresponding to the three regeneration steps as shown in figure 1. In

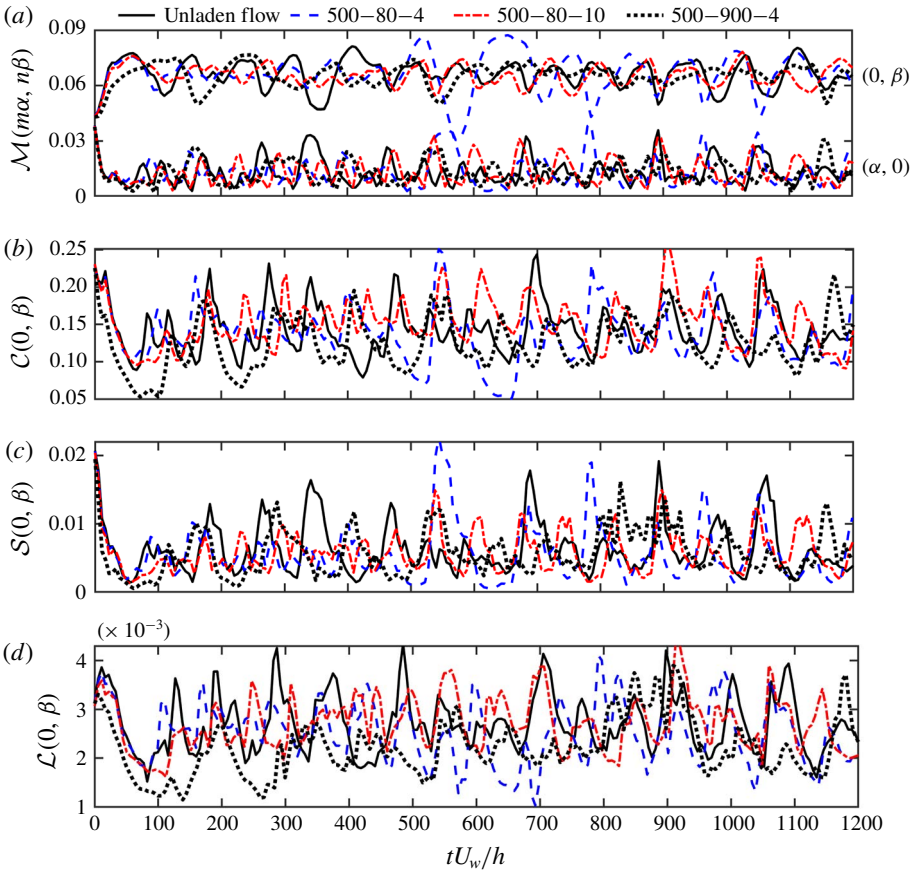

FIGURE 8. (Colour online) Modal decomposition of the various sub-steps composing the regeneration cycle as shown in figure 1 and outlined in § 4. Four cases are shown: 500–0–0 (unladen), 500–80 (500–80–4 and 500–80–10 with $St_{turb} = 0.056$, turbulence enhancement) and 500–900–4 ($St_{turb} = 0.625$, turbulence attenuation). (*a*) $\mathcal{M}(n\alpha, m\beta)$ as in (4.1) representing turbulent kinetic energy contained in the streaks; (*b*) $\mathcal{C}(0, \beta)$ as in (4.2) representing for the intensity of the LSV; (*c*) $\mathcal{S}(0, \beta)$ as in (4.5) representing the vorticity stretching effect to LSV; (*d*) $\mathcal{L}(0, \beta)$ representing the lift-up effect induced by LSV to enhance LSS as in (4.3). The initial 1200 time units (h/U_w) are shown.

single-phase flow, Hamilton *et al.* (1995) estimated this period is slightly less than 100 time units (h/U_w) at $Re_b = 500$. In flow influenced by low-inertia finite-size particles, Wang *et al.* (2017) also observed a similar period.

Figure 8 shows that the amplitudes of $\mathcal{M}(0, \beta)$ and $\mathcal{M}(\alpha, 0)$ are diminished by the inertial particles of case 500–900–4 (dotted black line), which is consistent with the behaviour observed by Wang *et al.* (2017) for finite-size particles. However for low particle inertia, the amplitude of $\mathcal{M}(\alpha, 0)$ is nearly unchanged due to low mass fraction (case 500–80–4) whereas it is suppressed with the presence of more particles of the same Stokes number (case 500–80–10). The presence of a large number of inertial particles (either when they enhance or attenuate the turbulence) tends to stabilize the amplitude of LSSs ($\mathcal{M}(0, \beta)$) but not significantly affect the time-averaged intensity of the streaks.

	$\mathcal{M}(0,\beta)$	$\mathcal{M}(\alpha,0)$	$\mathcal{C}(0,\beta)$	$\mathcal{L}(0,\beta)$	$\mathcal{S}(0,\beta)$
			Average $(\times 10^{-2})$		
Unladen flow	6.64	1.32	14.0	0.27	0.63
500–80–4	6.64	1.30	14.1	0.26	0.58
500–80–10	6.62	1.26	14.7	0.26	0.55
500–900–4	6.62	1.28	12.4	0.22	0.55
			Period (h/U_w)		
Unladen flow	104	104	104	99	104
500–80–4	94	89	99	89	94
500–80–10	89	84	80	84	84
500–900–4	121	121	121	105	116

TABLE 2. The average and period of five characteristic terms of the regeneration cycle. The error of the period due to the resolution of the signals is in the range of ± 2.5 time units.

The time-averaged intensities of $\mathcal{C}(0,\ \beta)$, $\mathcal{S}(0,\ \beta)$ and $\mathcal{L}(0,\ \beta)$ are provided in table 2, where we see that these characteristic terms are all suppressed when turbulence attenuation occurs due to particles (case 500–900–4). However, for cases with turbulence enhancement (cases 500–80–10 and 500–80–4), the primary difference is the amplified intensity of the circulation ($\mathcal{C}(0,\ \beta)$, also seen in figure 8*b*), and this amplification increases with particle concentration. The strengthened LSVs are critical for sustaining the turbulence and thus are consistent with the observed lower transitional Reynolds number ($Re_c \sim 290$ in case 500–80–4 versus $Re_c \sim 320$ for single-phase flow as shown in figure 3*a*). As found by Hamilton & Abernathy (1994), there is a minimum threshold of circulation below which the turbulence collapses and the flow becomes laminar. At lower Reynolds numbers and/or higher particle concentrations, we indeed see that this is the case (not shown here), and it appears that the primary effect of the particles is to modify the LSV strength during both stabilization and destabilization.

4.2. *Periodic behaviour and phase difference of the regeneration cycle*

To better understand the effects of particles on the timing of the regeneration cycle, we calculate a temporal autocorrelation of the five signals in figure 8:

$$R_{ss}(\Delta t) = \frac{\overline{s'(t)s'(t+\Delta t)}}{s'^2_{rms}}, \tag{4.6}$$

where s' is the fluctuation of a signal with respect to the time-averaged value.

The temporal autocorrelation is calculated over 3600 time units to ensure converged statistics. Figure 9(*a*) plots the five temporal autocorrelations in single-phase flow, case 500–80–4 is shown in figure 9(*b*) and case 500–900–4 is shown in figure 9(*c*). The time difference between the first two maxima of the correlation coefficient is taken as the period of the cycle and these are summarized in table 2. We can see that the period changes due to the presence of the particles, and that in cases of turbulence enhancement, the period is shortened (similar phenomenon is observed by Pan & Banerjee (1996), where particles enhance the turbulence with an increasing

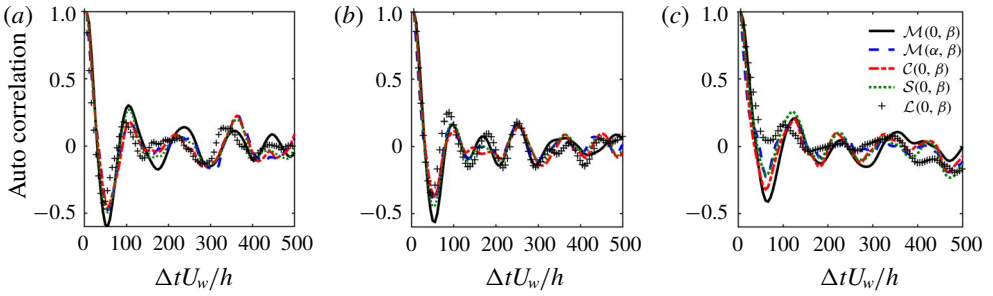

FIGURE 9. (Colour online) Temporal autocorrelation functions of the five signals shown in figure 8. (*a*) Single-phase flow, case 500–0–0. Suspension flow: (*b*) case 500–80–4; (*c*) case 500–900–4.

frequency of the sweep activity), while for turbulence suppression, the period is lengthened. Along these lines, in single-phase flow, Hamilton *et al.* (1995) observed that the period of the regeneration cycle is shortened at lower Reynolds numbers, e.g. 18 cycles in 1500 time units at $Re_b = 400$ versus 16 cycles in 1500 time units at $Re_b = 500$. Therefore comparing to single-phase flow, the period of the regeneration cycle increases in case 500–900–4 (turbulence is attenuated, behaving as a lower Reynolds in single-phase flow) whereas the period of the regeneration cycle decreases in cases 500–80–4 and 500–80–10 (turbulence is enhanced, behaving as a higher Reynolds in single-phase flow).

The regeneration cycle consists of three sequential sub-processes sketched in figure 1: streak formation, streak breakdown and streamwise vortex regeneration. The key mechanisms are: the LSSs are generated by a linear lift-up process by the LSVs, the LSSs break down to meandering streaks by complex nonlinear interactions and wavy streaks (x-dependent, contributing to $\partial u/\partial x$) interact with streamwise vorticity (ω_x) to strengthen the LSVs, which is another nonlinear process. This cycle is recognized as a robust, spatial–temporal evolution and time-stable self-sustaining process. We noted above that the period of this cycle (e.g. signal $\mathcal{M}(0,\beta)$) is around 104 time units in single-phase flow, 94 time units in case 500–80–4 and 121 time units in case 500–900–4. It is instructive to further analyse the phase difference during the regeneration cycle, especially in order to quantify the inertial particle effect during turbulence modulation. As can be seen in figure 8, the LSSs ($\mathcal{M}(0,\beta)$) and the meandering streaks ($\mathcal{M}(\alpha,0)$) nearly have opposite phase. Two subsequent sub-steps, the vortex stretching ($\mathcal{S}(0,\beta)$) and the lift-up ($\mathcal{L}(0,\beta)$) induced by LSVs, are closely synchronous with the temporal evolution of circulation ($\mathcal{C}(0,\beta)$). Vortex stretching, lift-up and circulation all seem to remain in phase with the meandering streaks. To verify this, we perform a temporal cross-correlation study of the five signals based on (4.7):

$$R_{s_1 s_2}(\Delta t) = \frac{\overline{s_1'(t+\Delta t)s_2'(t)}}{s_{1\,rms}' s_{2\,rms}'}, \tag{4.7}$$

where s_1' and s_2' are the fluctuations of signals s_1 and s_2 with respect to the time-averaged value. For instance, $R(\mathcal{M}(0,\beta),\mathcal{M}(\alpha,0))$ represents temporal cross-correlation between $\mathcal{M}(0,\beta)$ (LSS) and $\mathcal{M}(\alpha,0)$ (meandering streaks), thereby providing information on temporal lag between the two processes. If

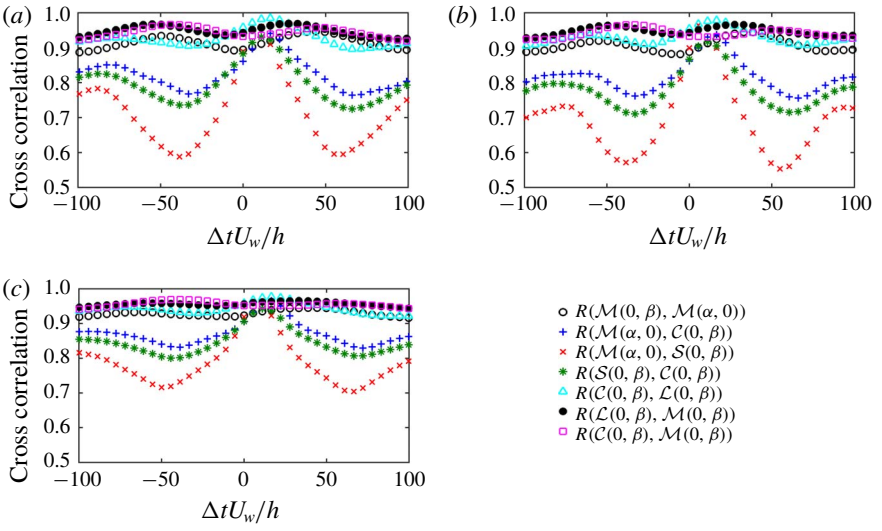

FIGURE 10. (Colour online) Temporal cross-correlation functions of the five signals shown in figure 8. (*a*) Single-phase flow, case 500–0–0. (*b*) Suspension flow, case 500–80–4. (*c*) Suspension flow, case 500–900–4. More than 3000 time units of phase shifts are calculated but only the range of −100 to 100 time units is shown.

	$\mathcal{M}(0,\beta),\mathcal{M}(\alpha,0)$	$\mathcal{M}(\alpha,0),\mathcal{C}$	$\mathcal{M}(\alpha,0),\mathcal{S}$	$\mathcal{S},\mathcal{C}$	$\mathcal{C},\mathcal{L}$	$\mathcal{L},\mathcal{M}$	$\mathcal{C},\mathcal{M}$
Unladen flow	40	17	8	11	17	30	44
500–80–4	34	16	6	11	11	30	40
500–80–10	28	16	6	11	16	28	34
500–900–4	44	17	8	11	17	38	58

TABLE 3. Time difference (time units) between connected sub-steps of the regeneration cycle. The error due to the resolution of the signals is in the range of ±2.5 time units.

$R(\mathcal{M}(0,\beta),\mathcal{M}(\alpha,0))$ is positive, it reflects that $\mathcal{M}(0,\beta)$ occurs prior in time to $\mathcal{M}(\alpha,0)$ during one regeneration cycle – the physical explanation for this specific case is that the LSS is formed, and subsequently breaks down into meandering streaks.

Figure 10 illustrates the phase difference between $\mathcal{M}(0,\beta)$, $\mathcal{M}(\alpha,0)$, $\mathcal{C}(0,\beta)$, $\mathcal{S}(0,\beta)$ and $\mathcal{L}(0,\beta)$ averaged over 3600 time units. Starting from the LSS ($\mathcal{M}(0,\beta)$) stage, we have chosen seven correlation coefficients between every pair of connected sub-steps. Figure 10(*a*) shows these coefficients for single-phase flow, in figure 10(*b*) for case 500–80–4 and in figure 10(*c*) for case 500–900–4. We quantify the phase shifts in table 3. Although inertial particles in case 500–900–4 have been found to attenuate the turbulence activity, the inertial particles actually do not significantly alter the basic regeneration cycle or its timing. The shortened or lengthened period of the regeneration cycle is mainly due to the particle modulation of streak breakdown from $\mathcal{M}(0,\beta)$ (LSS) to $\mathcal{M}(\alpha,0)$ (meandering streaks) and streak formation from $\mathcal{C}(0,\beta)$ (LSV) to $\mathcal{M}(0,\beta)$ (LSS). Here we should point out that the vortex regeneration is not necessary for every cycle; it might be absent for some cycles

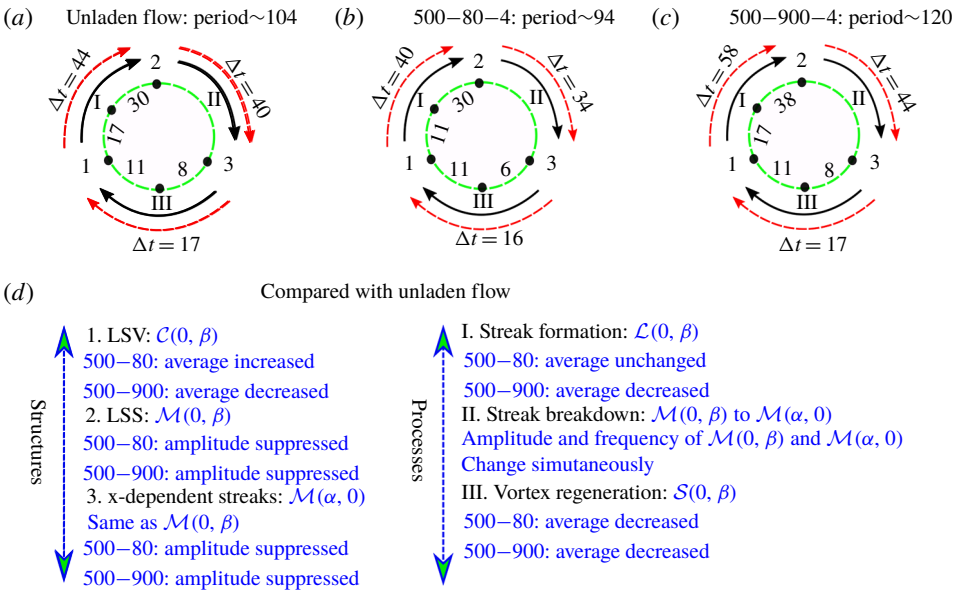

FIGURE 11. (Colour online) Sketch of phase difference between connected sub-steps and the period of the regeneration cycle in minimal unit: (*a*) case 500–0–0 in comparison with (*b*) case 500–80–4 and (*c*) case 500–900–4. (*d*) Qualitative comparison of the averaged value and the amplitude of the signals with single-phase flow.

(Hamilton *et al.* 1995), but its minimum value has to be above a threshold to produce unstable streaks.

Finally, we can summarize the primary effect of inertial particles on turbulence regeneration by continuing to use case 500–80 (including 500–80–4 and 500–80–10 with $St_{turb} = 0.056$) and case 500–900–4 ($St_{turb} = 0.625$) as representative examples of turbulence enhancement and turbulence attenuation, respectively. A temporal evolution of the regeneration cycle can be seen in the schematic sketch in figure 11(*a–c*). In this figure, we highlight the key turbulent structures and sub-steps by their corresponding metrics. The summation of the transition from $\mathcal{M}(0, \beta)$ to $\mathcal{M}(\alpha, 0)$, from $\mathcal{M}(\alpha, 0)$ to $\mathcal{C}(0, \beta)$ and from $\mathcal{C}(0, \beta)$ to $\mathcal{M}(0, \beta)$ yields roughly 101 time units in single-phase flow, 90 time units in case 500–80–4 and 119 time units in case 500–900–4 corresponding to the whole period 104 time units, 94 time units and 120 time units, respectively. Taking into consideration the resolution of signals, it is reasonable to believe that the summed phase differences are consistent with the calculated period of the regeneration cycle.

The regeneration cycle is therefore a temporal sequence of processes which has a stable periodicity, even under the influence of inertial particles – phase differences between linked sub-steps are nearly unchanged by the presence of particles except streak formation and breakdown. Instead, during turbulence enhancement (case 500–80), as can be seen in figure 11(*d*), the particles simply strengthen the magnitude of the LSVs ($\mathcal{C}(0, \beta)$), whereas during turbulence attenuation (case 500–900–4), the particles substantially reduce the magnitude of key turbulent structures and their corresponding sub-steps. Once the magnitude of the LSVs ($\mathcal{C}(0, \beta)$) is below a certain threshold (as in case 380–900–4), particles act to abruptly shut off the regeneration, thereby delaying turbulent-to-laminar transition. It is worth noting that a

similar upward shift of the transitional Reynolds owing to the vortex suppression is also observed during turbulence modulation laden with polymer additives – the modifications to the 'exact coherent states' are due to the suppression of the streamwise vortices due to the polymers exerting an opposite force to the fluid motion in the vortices and weakening the streamwise vortices (see Stone *et al.* 2004).

5. Concluding remarks

This work investigates the effect of inertial pointwise particles on the self-sustained process of the coherent structures in turbulent PCF. A 'miniunit' configuration with a low Reynolds number slightly above the onset of transition not only highlights the key turbulent structures making up the regeneration cycle, but can be simulated with much reduced computational cost. Two-way coupling of Lagrangian point particles with direct numerical simulations of Eulerian fluid flow is the methodology used in this work.

Through examining the particle inertial effect on transition, we find that lower particle inertia tends to advance the transition from laminar to turbulent flow whereas high particle inertia tends to delay the transition. These two limiting cases reflect the competition between the destabilization of the extra mixed-phase density and the stabilization due to the extra dissipation caused by the particle drag. While the nonlinear simulations capture features such as preferential accumulation, these results are in qualitative agreement with the previous linear stability analysis with assuming uniformly distributed particles. In agreement with other studies of particle-laden, wall-bounded turbulent flow, the particle response time alters where they tend to collect. The particle spatial distribution in turbulence is found to relate to the particle response time scaled by the characteristic LSV turnover time, which in turn affects the regeneration cycle. In the present domain, particles can reside either in the so-called LSS regions (high strain) or in the LSV regions (high vorticity). Low particle inertia (e.g. $St_{turb} = 0.056$) leads to long residence times in the same LSV, whereas high particle inertia (e.g. $St_{turb} = 0.625$) results in particles crossing the LSVs leading to a more homogeneous particle distribution. Between these extremes, particles with a moderate response time scale (e.g. $St_{turb} = 0.347$) are expelled from the LSVs and then collect in the LSSs leading to more particles accumulating in the near-wall region.

The particulate turbulent kinetic energy is highly related to particle spatial distribution and the associated slip velocity. Due to the preferential distribution of moderate-inertia particles (e.g. $St_{turb} = 0.347$) in the LSSs, the particulate turbulent kinetic energy is higher than that of the fluid in the streamwise direction whereas it is lower in wall-normal and spanwise directions. Particles with a large response time scale (e.g. $St_{turb} = 0.625$) cannot follow the streamlines, resulting in a more homogeneous distribution, which results in a more homogeneous turbulent kinetic energy of the particulate phase; however, it still exceeds the fluid phase kinetic energy in the steamwise direction.

Modal analysis is performed to examine the effect of the particles on the nonlinear regeneration cycle. For a representative set of cases at $Re_b = 500$, we quantitatively obtain its period to be roughly 104 time units in single-phase flow (case 500–0–0), whereas the period is around 94 time units in case 500–80–4 (turbulence enhancement happens in this case with $St_{turb} = 0.056$), and the period is around 121 time units in case 500–900–4 (turbulence attenuation happens in this case with $St_{turb} = 0.625$). Furthermore, the phase differences between the linked sub-steps are obtained based on

the maximum cross-correlation coefficient. The duration of each sub-step of the cycle as a fraction of the whole period of the regeneration cycle is about 43 % (respectively 44 % and 48 %) from LSV to LSS, 40 % (respectively 38 % and 38 %) from LSS to meandering streaks and 17 % (respectively 18 % and 14 %) from meandering streaks to LSV, in single-phase flow (respectively 500–80–4 and 500–900–4). The vortex regeneration process (from meandering streaks to LSV) is very fast whereas the lift-up process and streak breakdown process are relatively slow. The low-inertia particles (e.g. $St_{turb} = 0.056$) enhance the turbulence which shortens the period of the regeneration cycle whereas the high-inertia particles (e.g. $St_{turb} = 0.625$) attenuate the turbulence which lengthens the period of the regeneration cycle.

Even though inertial particles are found to have little effect on the phase differences between the linked sub-steps compared with the whole period, the intensity of circulation, lift-up and streamwise vorticity stretching are greatly suppressed (the reductions are about 15 % compared to single-phase flow in case 500–900–4) due to the presence of heavy inertial particles (e.g. $St_{turb} = 0.625$). The reduced intensity of circulation does not directly change the mean value of the streaks, while the amplitude of the LSSs is stabilized significantly due to the suppression of the LSVs following a suppressed lift-up effect. During turbulence attenuation by heavy inertial particles, the simulations show that it is streamwise particle–fluid coupling in an annulus region in the outer region of the LSVs coinciding with the region where streamwise vortex stretching is most active that plays the key role in suppressing the streamwise vortex stretching term and further deceasing the LSVs. However, during turbulence enhancement in cases 500–80, the circulation of LSVs is strengthened so that the minimum circulation threshold happens at a lower transition Reynolds number.

Acknowledgement

The authors acknowledge grant G00003613-ArmyW911NF-17-0366 from the US Army Research Office for financial support. Computational resources were provided by the Notre Dame Center for Research Computing. We are very grateful to Dr J. Capecelatro of the University of Michigan who provided valuable code validation resources and discussions. G.W. is grateful to Dr M. Abbas of Laboratoire de Génie Chimique (LGC) and Dr E. Climent of Institut de Mécanique des Fluides de Toulouse (IMFT) for very valuable discussions and constructive suggestions regarding the turbulent regeneration cycle and particle suspension flow.

Appendix A. Particle feedback effect on the near-wall vortex formation

The streamwise vorticity transport equation for an incompressible inviscid flow is expressed in (4.4). The vorticity stretching term $+\omega_x \partial u/\partial x$ represents the enhancement of vorticity and is responsible for the cascade process in turbulence. Sendstad & Moin (1992) found that the tilting term $-(\partial w/\partial x)(\partial u/\partial y)$ is the largest contribution to (4.4) close to the wall, and Hamilton *et al.* (1995) showed that the advection (redistribution) and stretching terms are responsible for the newly produced streamwise vorticity needed for LSV regeneration. In the work of Schoppa & Hussain (2002), they further qualitatively stated that the vortex formation is dominated by stretching of streamwise vorticity, because the spatial and temporal streamwise vortex collapse is in the necessary places associated with streamwise vorticity stretching. In particle-laden flow, due to the inhomogeneous distribution of the feedback force exerting from the particles to the fluid, an additional term $\partial F_z/\partial y - \partial F_y/\partial z$ needs to be considered as well.

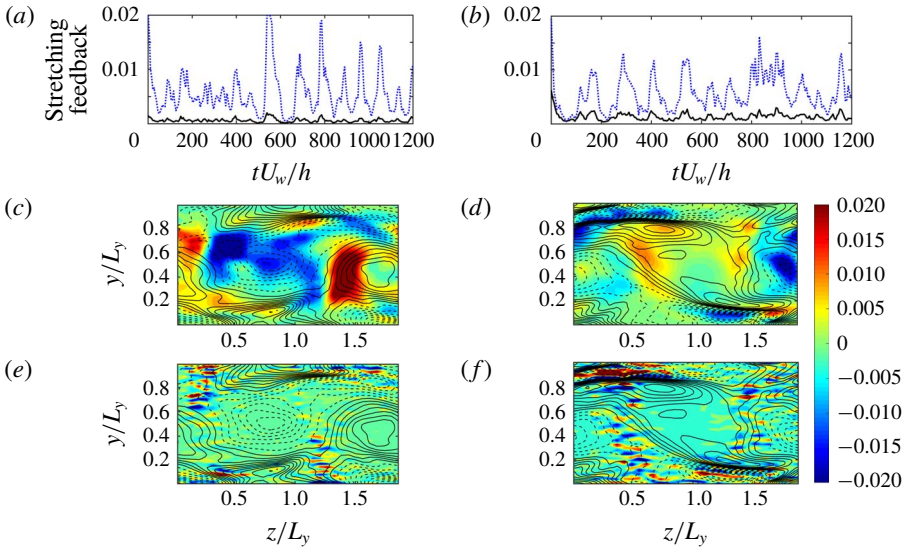

FIGURE 12. (Colour online) (*a*,*b*) Stretching term and particle feedback term contributions to equation (4.4) with $(0, \beta)$ integrated within $20 < y^+ < 60$. Dashed line: streamwise vortex stretching term. Solid line: particle feedback term. (*c*,*d*) Contour of temporal average of streamwise stretching term in one single cross-section (y, z plane) averaged over 50 time units. Included are isolines of temporal- and streamwise-averaged streamwise vorticity. Dashed line: negative streamwise vorticity. Solid line: positive streamwise vorticity. (*e*,*f*) Contour of the temporal average of the particle feedback term in one single cross-section (y, z plane) over 50 time units. Isolines are the same as they are in (*c*,*d*). (*a*,*c*,*e*) Case 500–80–4. (*b*,*d*,*f*) Case 500–900–4.

We compare the temporal evaluation of the stretching term and particle feedback terms in figure 12(*a*,*b*) along with their spatial distributions in the (y, z) plane in figure 12(*c*–*f*). Figure 12(*a*,*c*,*e*) and figure 12(*b*,*d*,*f*) show case 500–80–4 and case 500–900–4, respectively. In figure 12(*a*,*b*), we plot the amplitudes of both stretching term and particle feedback term contributing to the LSV with mode $(0, \beta)$. We find that the evolution of the particle feedback term is synchronous with the stretching term. However, compared with the stretching term (considered to be the main contribution to the regeneration of streamwise vorticity), the direct contribution from the particle feedback term is relatively small due to the low mass loading (about 10 % in case 500–80–4 and 17 % in case 500–900–4). However, whether the location of the particle feedback term coincides with the streamwise vorticity formation is still unclear. In figure 12(*e*,*f*), we time-average (50 time units) the particle feedback term at a single cross-section at $x = L_x/2$. The particle feedback term is active between the negative and positive streamwise vorticity region, where the region is filled by streaks. In streaks, the particle feedback term occurs with alternate positive and negative values. It is not only in the locations where the streamwise vorticity is strengthened. As a comparison, we show the stretching term in figure 12(*c*,*d*), where the location of ω_x stretching coincides with the streamwise vorticity, which is responsible for the vortex formation.

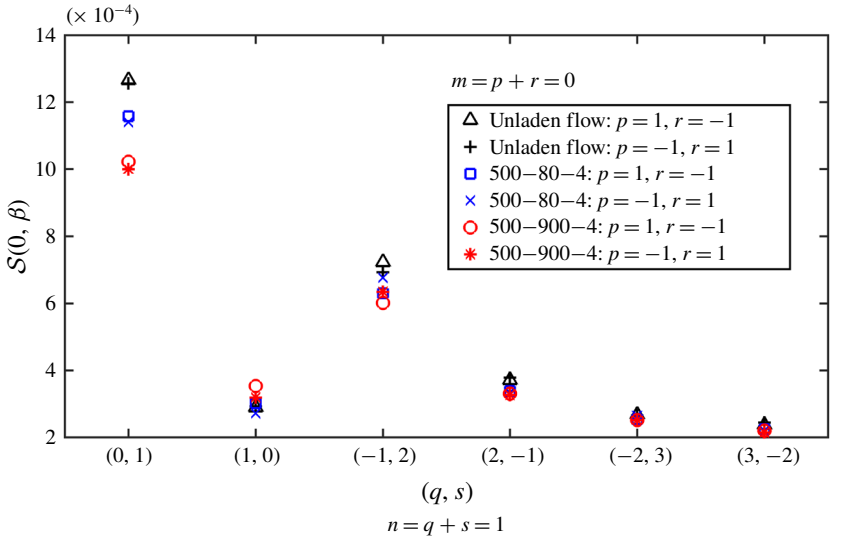

FIGURE 13. (Colour online) Temporal average intensity of vorticity stretching term in (4.5) of 12 pairs of modes. Comparison between single-phase flow (500–0–0) and suspension flow (500–80–4 and 500–900–4).

Appendix B. Particle effects on 12 modes of vorticity stretching term

In the modal analysis of the regeneration cycle, the generation of streamwise vorticity is mainly caused by the streamwise vortex stretching term $\widehat{\omega}_x(p\alpha, q\beta)\partial\widehat{u}_x(r\alpha, s\beta)/\partial x$ in Fourier space, where p, q, r, s must satisfy $p + r = m$ and $q + s = n$. The maximum circulation is always due to the x-independent streamwise vorticity with mode $(0, \beta)$ based on our observations. Therefore even though it is only the relations $p + r = 0$ and $q + s = 1$ which contribute to $\partial\widehat{\omega}_x(0, \beta)/\partial t$, there are still $(N_x - 1)(N_z - 2)$ pairs of $\widehat{\omega}_x(p\alpha, q\beta)$ and $\partial\widehat{u}_x(r\alpha, s\beta)/\partial x$ to be examined. In the streamwise direction, the work of Hamilton *et al.* (1995) has simplified the above relation to α-modes ($p = \pm 1$ and $r = \mp 1$ satisfy $m = p + r = 0$) dominant relation where the higher x-wavenumber mode ($|p| > 1$ and $|r| > 1$ satisfy $m = p + r = 0$) contributions to $\partial\widehat{\omega}_x(0, \beta)/\partial t$ are negligible. Furthermore, we have compared all $(N_z - 2)$ spanwise combinations satisfying $n = q + s = 1$ and then find the main contribution in the spanwise direction as $q = -2$ to 3 combining with $s = 3$ to -2 satisfying relation $q + s = 1$, which are used to represent the vorticity stretching term in this work (total of 12 pairs of x and z wavenumbers).

Figure 13 plots the wall-normal integrated modulus of vorticity stretching in (4.5) for the 12 modes for cases 500–0–0, 500–80–4 and 500–900–4. We can see that for the same z wavenumber, the integrated modulus of vorticity stretching is similar between $p = 1, r = -1$ and $p = -1, r = 1$. On the other hand, the contribution from modes $q = 0, s = 1$ and $q = -1, s = 2$ reflects 64 %, 61 % and 58 % of the total modulus of all wavenumbers in single-phase flow, case 500–80–4 and case 500–900–4, respectively.

Figure 14 shows the phase difference between $\mathcal{M}(\alpha, 0)$ (meandering streaks contributing to $\partial u/\partial x$) with six pairs of mode q, s with fixed $p = 1, r = -1$ (the other six pairs of mode q, s with fixed $p = -1, r = 1$ give similar results). Except when the phase difference is about 8 time units for $q = 0, s = 1$, all others are in the

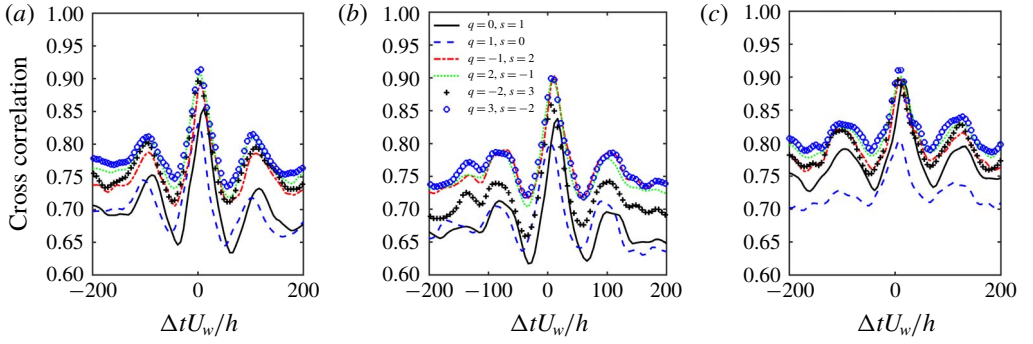

FIGURE 14. (Colour online) Phase shifts between vorticity stretching term (six pairs of modes with fixed $p=1, r=-1$) with the meander streak $\mathcal{M}(\alpha, 0)$. (*a*) Single-phase flow (500–0–0). Particle-laden flow: (*b*) case 500–80–4 and (*c*) case 500–900–4.

range of 0–5 time units. We do the summation of all these signals (both modulus and argument angle) to produce figure 10.

REFERENCES

BALACHANDAR, S. & EATON, J. K. 2010 Turbulent dispersed multiphase flow. *Annu. Rev. Fluid. Mech.* **42**, 111–133.

BECH, K. H., TILLMARK, N., ALFREDSSON, P. H. & ANDERSSON, H. I. 1995 An investigation of turbulent plane Couette flow at low Reynolds numbers. *J. Fluid Mech.* **286**, 291–326.

BRANDT, L. 2014 The lift-up effect: the linear mechanism behind transition and turbulence in shear flows. *Eur. J. Mech.* (B/*Fluids*) **47**, 80–96.

BURTON, T. M. & EATON, J. K. 2005 Full resolved simulations of particle–turbulence interaction. *J. Fluid Mech.* **545**, 67–111.

CAPECELATRO, J. & DESJARDINS, O. 2013 An Euler–Lagrange strategy for simulating particle-laden flows. *J. Comput. Phys.* **238**, 1–31.

CAPECELATRO, J., DESJARDINS, O. & FOX, R. O. 2018 On the transition between turbulence regimes in particle-laden channel flows. *J. Fluid Mech.* **845**, 499–519.

DESPIRITO, J. & WANG, L.-P. 2001 Linear instability of two-way coupled particle-laden jet. *Intl J. Multiphase Flow* **27** (7), 1179–1198.

DIMAS, A. & KIGER, K. 1998 Linear instability of a particle-laden mixing layer with a dynamic dispersed phase. *Phys. Fluids* **10** (10), 2539–2557.

DRITSELIS, C. D. & VLACHOS, N. S. 2008 Numerical study of educed coherent structures in the near-wall region of a particle-laden channel flow. *Phys. Fluids* **20** (5), 055103.

DRUZHININ, O. & ELGHOBASHI, S. 1998 Direct numerical simulations of bubble-laden turbulent flows using the two-fluid formulation. *Phys. Fluids* **10** (3), 685–697.

EATON, J. K. & FESSLER, J. 1994 Preferential concentration of particles by turbulence. *Intl J. Multiphase Flow* **20**, 169–209.

ELGHOBASHI, S. 1994 On predicting particle-laden turbulent flows. *Appl. Sci. Res.* **52** (4), 309–329.

ELGHOBASHI, S. & TRUESDELL, G. 1993 On the two-way interaction between homogeneous turbulence and dispersed solid particles. I. Turbulence modification. *Phys. Fluids* A **5** (7), 1790–1801.

ELLINGSEN, T. & PALM, E. 1975 Stability of linear flow. *Phys. Fluids* **18** (4), 487–488.

GARRATT, J. R. 1994 The atmospheric boundary layer. *Earth-Sci. Rev.* **37** (1–2), 89–134.

GORE, R. & CROWE, C. T. 1989 Effect of particle size on modulating turbulent intensity. *Intl J. Multiphase Flow* **15** (2), 279–285.

GUALTIERI, P., PICANO, F., SARDINA, G. & CASCIOLA, C. M. 2015 Exact regularized point particle method for multiphase flows in the two-way coupling regime. *J. Fluid Mech.* **773**, 520–561.

HAMILTON, J. M. & ABERNATHY, F. H. 1994 Streamwise vortices and transition to turbulence. *J. Fluid Mech.* **264**, 185–212.

HAMILTON, J. M., KIM, J. & WALEFFE, F. 1995 Regeneration mechanisms of near-wall turbulence structures. *J. Fluid Mech.* **287**, 317–348.

INOUE, M., MATHIS, R., MARUSIC, I. & PULLIN, D. 2012 Inner-layer intensities for the flat-plate turbulent boundary layer combining a predictive wall-model with large-eddy simulations. *Phys. Fluids* **24** (7), 075102.

JIMÉNEZ, J. 2018 Coherent structures in wall-bounded turbulence. *J. Fluid Mech.* **842**, P1.

JIMÉNEZ, J. & MOIN, P. 1991 The minimal flow unit in near-wall turbulence. *J. Fluid Mech.* **225**, 213–240.

JIMÉNEZ, J. & PINELLI, A. 1999 The autonomous cycle of near-wall turbulence. *J. Fluid Mech.* **389**, 335–359.

KAWAHARA, G. & KIDA, S. 2001 Periodic motion embedded in plane Couette turbulence: regeneration cycle and burst. *J. Fluid Mech.* **449**, 291–300.

KITOH, O., NAKABYASHI, K. & NISHIMURA, F. 2005 Experimental study on mean velocity and turbulence characteristics of plane Couette flow: low-Reynolds-number effects and large longitudinal vortical structure. *J. Fluid Mech.* **539**, 199–227.

KLINKENBERG, J., DE LANGE, H. & BRANDT, L. 2011 Modal and non-modal stability of particle-laden channel flow. *Phys. Fluids* **23** (6), 064110.

KLINKENBERG, J., DE LANGE, H. & BRANDT, L. 2014 Linear stability of particle laden flows: the influence of added mass, fluid acceleration and Basset history force. *Meccanica* **49** (4), 811–827.

KLINKENBERG, J., SARDINA, G., DE LANGE, H. & BRANDT, L. 2013 Numerical study of laminar-turbulent transition in particle-laden channel flow. *Phys. Rev.* E **87** (4), 043011.

KOMMINAHO, J., LUNDBLADH, A. & JOHANSSON, A. V. 1996 Very large structures in plane turbulent Couette flow. *J. Fluid Mech.* **320**, 259–285.

LEE, J. & LEE, C. 2015 Modification of particle-laden near-wall turbulence: effect of Stokes number. *Phys. Fluids* **27** (2), 023303.

LI, Y., MCLAUGHLIN, J. B., KONTOMARIS, K. & PORTELA, L. 2001 Numerical simulation of particle-laden turbulent channel flow. *Phys. Fluids* **13** (10), 2957–2967.

MAJJI, M. V., BANERJEE, S. & MORRIS, J. F. 2018 Inertial flow transitions of a suspension in Taylor–Couette geometry. *J. Fluid Mech.* **835**, 936–969.

MARCHIOLI, C. & SOLDATI, A. 2002 Mechanisms for particle transfer and segregation in a turbulent boundary layer. *J. Fluid Mech.* **468**, 283–315.

MASSOT, M. 2007 Eulerian multi-fluid models for polydisperse evaporating sprays. In *Multiphase Reacting Flows: Modelling and Simulation*, pp. 79–123. Springer.

MATAS, J.-P., MORRIS, J. F. & GUAZZELLI, E. 2003 Transition to turbulence in particulate pipe flow. *Phys. Rev. Lett.* **90**, 014501.

MAXEY, M. 1987 The motion of small spherical particles in a cellular flow field. *Phys. Fluids* **30** (7), 1915–1928.

MAXEY, M. R. & RILEY, J. J. 1983 Equation of motion for a small rigid sphere in a nonuniform flow. *Phys. Fluids* **26** (4), 883–889.

MICHAEL, D. 1964 The stability of plane poiseuille flow of a dusty gas. *J. Fluid Mech.* **18** (1), 19–32.

PAN, Y. & BANERJEE, S. 1996 Numerical simulation of particle interactions with wall turbulence. *Phys. Fluids* **8** (10), 2733–2755.

POPE, S. B. 2000 *Turbulent Flows*. Cambridge University Press.

RICHTER, D. H. 2015 Turbulence modification by inertial particles and its influence on the spectral energy budget in planar Couette flow. *Phys. Fluids* **27** (6), 063304.

RICHTER, D. H. & SULLIVAN, P. P. 2013 Momentum transfer in a turbulent, particle-laden Couette flow. *Phys. Fluids* **25** (5), 053304.

RICHTER, D. H. & SULLIVAN, P. P. 2014 Modification of near-wall coherent structures by inertial particles. *Phys. Fluids* **26** (10), 103304.

RUDYAK, V. Y., ISAKOV, E. & BORD, E. 1998 Instability of plane Couette flow of two-phase liquids. *Tech. Phys. Lett.* **24** (3), 199–200.

RUDYAK, V. Y., ISAKOV, E. B. & BORD, E. G. 1997 Hydrodynamic stability of the Poiseuille flow of dispersed fluid. *J. Aero. Sci.* **28** (1), 53–66.

SAFFMAN, P. 1962 On the stability of laminar flow of a dusty gas. *J. Fluid Mech.* **13** (1), 120–128.

SARDINA, G., SCHLATTER, P., BRANDT, L., PICANO, F. & CASCIOLA, C. M. 2012 Wall accumulation and spatial localization in particle-laden wall flows. *J. Fluid Mech.* **699**, 50–78.

SCHILLER, V. 1933 Ber die grundlegenden berechnungen bei der schwerkraftaufbereitung. *Z. Verein. Deutsch. Ing.* **77**, 318–321.

SCHOPPA, W. & HUSSAIN, F. 2002 Coherent structure generation in near-wall turbulence. *J. Fluid Mech.* **453**, 57–108.

SENDSTAD, O. & MOIN, P. 1992 The near-wall mechanics of three-dimensional boundary layers. Report tf-57. Thermoscience Division, Department of Mechanical Engineering.

SMITS, A. J., MCKEON, B. J. & MARUSIC, I. 2011 High–Reynolds number wall turbulence. *Annu. Rev. Fluid Mech.* **43**, 353–375.

SQUIRES, K. D. & EATON, J. K. 1990 Particle response and turbulence modification in isotropic turbulence. *Phys. Fluids* A **2** (7), 1191–1203.

STONE, P. A., ROY, A., LARSON, R. G., WALEFFE, F. & GRAHAM, M. D. 2004 Polymer drag reduction in exact coherent structures of plane shear flow. *Phys. Fluids* **16** (9), 3470–3482.

SWEET, J., RICHTER, D. H. & THAIN, D. 2018 GPU acceleration of Eulerian–Lagrangian particle-laden turbulent flow simulations. *Intl J. Multiphase Flow* **99**, 437–445.

TANAKA, T. & EATON, J. K. 2008 Classification of turbulence modification by dispersed spheres using a novel dimensionless number. *Phys. Rev. Lett.* **101** (11), 114502.

WALEFFE, F. 1997 On a self-sustaining process in shear flows. *Phys. Fluids* **9** (4), 883–900.

WANG, G., ABBAS, M. & CLIMENT, E. 2017 Modulation of large-scale structures by neutrally buoyant and inertial finite-size particles in turbulent Couette flow. *Phys. Rev. Fluids* **2** (8), 084302.

WANG, G., ABBAS, M. & CLIMENT, E. 2018 Modulation of the regeneration cycle by neutrally buoyant finite-size particles. *J. Fluid Mech.* **852**, 257–282.

YU, W., VINKOVIC, I. & BUFFAT, M. 2016 Finite-size particles in turbulent channel flow: quadrant analysis and acceleration statistics. *J. Turbul.* **17** (11), 1048–1071.

ZHAO, L., ANDERSSON, H. I. & GILLISSEN, J. J. 2013 Interphasial energy transfer and particle dissipation in particle-laden wall turbulence. *J. Fluid Mech.* **715**, 32–59.